Computer Physics Communications 185 (2014) 1965–1980

Contents lists available at ScienceDirect

Computer Physics Communications

journal homepage: www.elsevier.com/locate/cpc

SIP-CESE MHD model of solar wind with adaptive mesh refinement of hexahedral meshes

Xueshang Feng *, Changqing Xiang, Dingkun Zhong, Yufen Zhou, Liping Yang, Xiaopeng Ma

SIGMA Weather Group, State Key Laboratory for Space Weather, Center for Space Science and Applied Research, Chinese Academy of Sciences, Beijing 100190, China

ARTICLE INFO

Article history:
Received 3 January 2014
Received in revised form
18 March 2014
Accepted 26 March 2014
Available online 3 April 2014

Keywords:
Solar wind
Magnetohydrodynamics (MHD)
Numerical simulation

ABSTRACT

Solar–interplanetary space involves many features, such as discontinuities and heliospheric current sheet, with spatial scales many orders of magnitude smaller than the system size. The scalable, massively parallel, block-based, adaptive-mesh refinement (AMR) promises to resolve different temporal and spatial scales on which solar-wind plasma occurs throughout the vast solar–interplanetary space with even less cells but can generate a good enough resolution. Here, we carry out the adaptive mesh refinement (AMR) implementation of our Solar–Interplanetary space–time conservation element and solution element (CESE) magnetohydrodynamic model (SIP-CESE MHD model) using a six-component grid system (Feng et al., 2007, 2010). The AMR realization of the SIP-CESE MHD model is naturalized directly in hexahedral meshes with the aid of the parallel AMR package PARAMESH available at http://sourceforge.net/projects/paramesh/. At the same time, the topology of the magnetic field expansion factor and the minimum angular separation (at the photosphere) between an open field foot point and its nearest coronal-hole boundary are merged into the model in order to determine the volumetric heating source terms. Our numerical results for the validation study of the solar-wind background of Carrington rotation 2060 show overall good agreements in the solar corona and in interplanetary space with the observations from the Solar and Heliospheric Observatory (SOHO) and spacecraft data from OMNI.

1. Introduction

It is believed that presently, and in the foreseeable future, three-dimensional (3D) global magnetohydrodynamic (MHD) models are the only models that can span the enormous distances present in the corona–interplanetary space, although even generalized MHD equations are only a relatively low-order approximation to more complete physics by providing only a simplified description of natural phenomena in space plasmas.

In quantitatively modeling the solar wind structures and their interactions with magnetosphere–ionosphere system, 3D global MHD-based high performance computational models have been developed by many researches (e.g [1–31]). There are several global MHD models based on numerous modern well-known schemes of modeling the corona–interplanetary space, to say a few for reference to a number of such studies: Flux Corrected Transport (FCT) [32,33], Total Variation Diminishing (TVD) schemes [13,17,18] and the monotonic upstream scheme for conservation laws (MUSCL) [34,35], Roe type scheme [8,20,36,37], a mixed scheme of a finite-difference discretization for the radial and axial coordinates combined with a pseudospectral method for the azimuthal coordinate [1,38,39], Essentially Non-oscillatory (ENO) schemes [40], the Van Leer flux limited schemes and conservation element and solution element (CESE) [12,15,29,31], and the so-called Harten–Lax–van Leer (HLL) type [29,41,42]. For survey of progress made in the numerical space weather modeling from the Sun to Earth or beyond, we can refer to [43–47].

In a series of papers [12,15,29,31,48–60], Feng and his colleagues have developed a 3D MHD model to investigate solar-terrestrial physical phenomena and space weather study based on the space–time conservation element and the solution element (CESE) method (hereafter called the SIP-CESE MHD model for brief). In what follows, we mention some results achieved up to now by the SIP-CESE MHD model.

With the purpose of operational real-time forecasting for arrival times of flare/coronal mass ejection associated shocks in the vicinity of the Earth, Feng et al. [51] established a one-dimensional hydrodynamic (HD) shock propagation model by the

* Corresponding author.
E-mail address: fengx@spaceweather.ac.cn (X. Feng).

http://dx.doi.org/10.1016/j.cpc.2014.03.027
0010-4655/

CESE method. The required observational data inputs to this new one-dimensional CESE-HD model are the shock speed from the frequency drift rate of type II radio burst in low corona, the duration estimation, and the background solar wind speed for a solar eruptive event. Applying this model to 137 solar events during the period of February 1997 to August 2002, it is found that their model could be practically equivalent to the four commonly used models in forecasting the shock arrival time, namely the Shock Time of Arrival Model (STOA); the Interplanetary Shock Propagation Model (ISPM), the Hakamada–Akasofu–Fry (HAFv.2) model, and the Shock Propagation Model (ISPM). The absolute error in the transit time from their model is not larger than those of the other four models for the same set of events.

Feng et al. [15] employed SIP-CESE MHD model within a six-component overset grid for solar wind simulation. The essential merits are as follows: (1) the removal of the singularity and mesh convergence near the poles via the use of the six-component grid system, (2) the $\nabla \cdot \mathbf{B}$ constraint error via an easy-to-use cleaning procedure by a fast multigrid Poisson solver, (3) the mitigation of the Courant–Friedrichs–Levy number disparity via the Courant-number insensitive method, (4) the use of time integration by multiple time stepping, and (5) the application of time-dependent characteristic boundary condition at the subsonic region by limiting the mass flux escaping through the solar surface. In order to produce fast and slow plasma streams of the solar wind, they include the volumetric heating source terms and momentum addition by involving the topological effect of the magnetic field expansion factor f_s and the minimum angular distance θ_b (at the photosphere) between an open field foot point and its nearest coronal hole boundary.

A hybrid three-dimensional (3D) MHD model for solar wind study is proposed by Feng et al. [29] with combined grid systems and solvers. The computational domain from the Sun to Earth space is decomposed into the near-Sun and off-Sun domains, which are respectively constructed with a Yin–Yang overset grid system and a Cartesian adaptive mesh refinement (AMR) grid system and coupled with a domain connection interface in the overlapping region between the near-Sun and off-Sun domains. The space–time CESE method is used in the near-Sun domain, while the Harten–Lax–Leer method is employed in the off-Sun domain. The Yin–Yang overset grid can avoid well-known singularity and polar grid convergence problems and its body-fitting property helps achieve high-quality resolution near the solar surface. The block structured AMR Cartesian grid can automatically capture far-field plasma flow features, such as heliospheric current sheets and shock waves, and at the same time, it can save significant computational resources compared to the uniformly structured Cartesian grid.

Feng et al. [31] carried out the adaptive mesh refinement (AMR) implementation of the SIP-CESE MHD model within a six-component grid system. By transforming the governing MHD equations from the physical space (x, y, z) to the computational space (ξ, η, ζ) while retaining the conservation form, the AMR of SIP-MHD model is implemented in the reference coordinates with the aid of the parallel AMR package PARAMESH available at http://sourceforge.net/projects/paramesh/. To study the dynamic evolution of the global corona, Feng et al. [55], Yang et al. [58], Feng et al. [60] developed a time-dependent MHD model driven by the daily-updated synoptic magnetograms with the help of the 3D Solar–Interplanetary (SIP) adaptive mesh refinement (AMR) space–time conservation element and solution element (CESE) MHD model (SIP-AMR-CESE MHD Model).

By using the 3D SIP-CESE MHD model, Zhou et al. [49,57] and Zhou and Feng [50] studied the evolution of the Sun–Earth connection coronal mass ejections (CMEs) on 12 May 1997, 4 November, 1997, and three successive CMEs of November 4–5, 1998. The results proved a relatively satisfactory comparison with the Wind spacecraft observations, such as southward interplanetary magnetic field and large-scale smooth rotation of the magnetic field associated with the CMEs.

With 3D SIP-CESE MHD model, Yang et al. [54,61] simulated the unusual solar minimum by comparison with multi-satellite observations, and studied the heating effects of solar wind by comparing the Wentzel–Kramers–Brillouin (WKB) Alfvén wave heating method, the turbulence heating method and the volumetric heating method.

By employing the CESE scheme with the full MHD equations, Jiang et al. [52,53,62] and Jiang and Feng [56,63] presented a new implementation of the MHD relaxation method for reconstruction of the nearly force-free coronal magnetic field from a photospheric vector magnetogram. The bottom boundary condition is prescribed in a similar way as in the stress-and-relax method, by changing the transverse field incrementally to match the magnetogram, and other boundaries of the computational box are set by the nonreflecting boundary conditions [53]. Applications to the well-known benchmarks for nonlinear force-free-field reconstruction, the force-free equilibria, validate the method and confirm its capability for future practical application with observed magnetograms as inputs.

In summary, the SIP-CESE MHD model developed by Feng and his colleagues [12,15,29,31,48–54,56–59,64] has the following merits.

(i) The new implementation of volumetric heating source term taking the topological effect of magnetic field with the expansion factor f_s and the angular distance θ_b into consideration, to some extent, can effectively distinguish the high-speed solar wind from the low-speed solar wind.

(ii) The combination of the projected normal characteristic method and the mass flux limit enables the model to reproduce reasonable distributions of the plasma density, temperature and velocity on the solar surface and incorporation of the time-dependent magnetograms into the model is preliminarily established [55,58,60], with emphasis focused on how to preprocess the observational data, how to solve projected normal characteristics equations, and how to update the bottom boundary by using the time-dependent magnetic field from either observations or the surface flux transport model.

(iii) The model provides a unified treatment of flow evolution in space and time and keeps the local and global space–time flux conservation in a coherent and efficient manner.

(iv) The solution points in SIP-CESE MHD model [31,52] are explicitly given on the mesh nodes, while formerly these points have to be calculated after setting the grids and the projection of the CE onto the spatial space has been greatly simplified to a rectangular cuboid. Therefore, the fluxes at the interface of any pair of conservation elements (CEs) can be efficiently evaluated by means of non-staggered space–time grids without using Riemann solvers or other flux models, which significantly reduces the CPU time.

(v) The treatment of time iteration by integrating two half timesteps into one full timestep leads to low-storage and makes the scheme suitable for building blocks for adaptive mesh refinement calculations.

(vi) The introduction of six-component grid for the computational domain from the Sun to Earth or beyond enables us to fit the spherical surface boundary with an easy implementation of the inner boundary conditions, and meanwhile to avoid both coordinate singularities and polar grid convergence. Particularly, it will be easy to recognize the observation at the lower boundary.

(vii) Through the use of nonsingular transform from the physical space to the reference space, the quadrangular frustum pyramid cell for the spherical shell computational domain for solar wind modeling becomes the conventional rectangular box in the reference space (ξ, η, ζ), which can be seen as the usual Cartesian

coordinate. Consequently, the AMR implementation of the code follows easily from PARAMESH in Cartesian coordinate. Thus, besides the CESE scheme, many other modern numerical schemes in Cartesian coordinate such as total variation diminishing (TVD) scheme and finite volume method (FVM) can be applied directly to the transformed system. This feature provides us many flexible alternatives of solving the transformed governing equations in (ξ, η, ζ) and then we recover the solution in the physical space through the transformation to obtain the solar wind solution.

(ix) It should be noted that the same CESE solver can apply to any coordinate system (such as Cartesian, spherical, cylindrical coordinates and any other curvilinear coordinates) with only the difference of the coordinate transformation, and consequently the solver is highly independent of the grid system.

(x) Based on the CESE MHD model, the new implementation of the MHD relaxation method [52–54,56,59,63] for reconstruction of coronal magnetic field from a photospheric vector magnetogram will open a new way for the study of solar active region with the help of SDO/HMI or SOHO/MDI observations [62].

Corona–interplanetary space involves the presence of different temporal and spatial scales on which solar wind plasma occurs throughout the vast solar–interplanetary space, and contains many critical features, such as discontinuities and heliospheric current sheet, that have spatial scales many orders of magnitude smaller than the system size. The numerical grids are either adapted to the small scale features in the system, or a brute force approach is used with as high numerical resolution as possible while fighting the limits of available computational power. Adaptive mesh refinement (AMR) promises to be capable of better resolving the solution features of these flows with even less cells but may generate a substantial computational overhead due to the remeshing, refluxing at coarse–fine interfaces, and guardcell filling.

In the present paper, the AMR realization of SIP-CESE MHD model is naturalized directly in hexahedral meshes with the aid of the parallel AMR package PARAMESH available at http://sourceforge.net/projects/paramesh/. First, the governing equations for solar wind plasma is described and the CESE method in hexahedral meshes is given for self-consistence. Then, the model is validated by the numerical study of the solar-wind background of Carrington rotation (CR) 2060 with comparison in the solar corona and in interplanetary space with SOHO observation and spacecraft data from OMNI. Finally, a conclusion is made.

2. SIP-CESE MHD model

The basic equations governing the solar wind evolution are the set of the MHD equations in the conservative form given [15,31]

$$
\begin{aligned}
&\frac{\partial \rho}{\partial t} + \nabla \cdot \rho \mathbf{u} = 0\\
&\frac{\partial \rho \mathbf{u}}{\partial t} + \nabla \cdot \left[\rho \mathbf{u}\mathbf{u} + \mathbf{I}\left(p + \frac{1}{2}\mathbf{B}_1^2 + \mathbf{B}_1 \cdot \mathbf{B}_0\right) \right.\\
&\qquad \left. - \mathbf{B}_1\mathbf{B}_1 - \mathbf{B}_1\mathbf{B}_0 - \mathbf{B}_0\mathbf{B}_1 \right]\\
&\quad = \mathbf{j}_0 \times \mathbf{B}_0 + \rho\left[\mathbf{g} - \boldsymbol{\Omega} \times (\boldsymbol{\Omega} \times \mathbf{r})\right] - 2\rho\boldsymbol{\Omega} \times \mathbf{u} + \mathbf{S}_m,\\
&\frac{\partial e_1}{\partial t} + \nabla \cdot \left[\mathbf{u}\left(e_1 + p + \frac{1}{2}\mathbf{B}_1^2 + \mathbf{B}_1 \cdot \mathbf{B}_0\right) - (\mathbf{u} \cdot \mathbf{B}_1)(\mathbf{B}_1 + \mathbf{B}_0) \right]\\
&\quad = -\mathbf{B}_1 \cdot \frac{\partial \mathbf{B}_0}{\partial t} + \mathbf{E} \cdot \mathbf{j}_0\\
&\qquad + \rho\mathbf{u} \cdot \left[\mathbf{g} - \boldsymbol{\Omega} \times (\boldsymbol{\Omega} \times \mathbf{r})\right] + Q_e + \mathbf{u} \cdot \mathbf{S}_m,\\
&\frac{\partial \mathbf{B}_1}{\partial t} + \nabla \cdot (\mathbf{u}\mathbf{B} - \mathbf{B}\mathbf{u}) = -\frac{\partial \mathbf{B}_0}{\partial t}
\end{aligned}
\tag{1}
$$

with

$$
\mathbf{E} = \mathbf{u} \times \mathbf{B}, \qquad \mathbf{j}_0 = \nabla \times \mathbf{B}_0, \quad \text{and} \quad e_1 = \frac{1}{2}\rho\mathbf{u}^2 + \frac{p}{\gamma - 1} + \frac{1}{2}\mathbf{B}_1^2
$$

where e_1 corresponds to the modified total energy density consisting of the kinetic, thermal, and magnetic energy density (written in terms of $\mathbf{B}_1$). A factor of $1/\sqrt{\mu}$ is included in the definition of $\mathbf{B}$, and $\mathbf{B}_0$ is constant in time.

Here, ρ is the mass density, $\mathbf{u} = (u, v, w)$ are the velocities in x, y, and z directions, p is the thermal pressure, and $\mathbf{B} = \mathbf{B}_0 + \mathbf{B}_1$ denotes the total magnetic field consisting of the time-independent potential magnetic field $\mathbf{B}_0$ and its time-dependent derived part $\mathbf{B}_1$ by employing the technique of splitting the magnetic field as done by Tanaka [17] and [15,31] to improve the accuracy of the simulated magnetic field. t and $\mathbf{r}$ are time and position vector originating at the center of the Sun, $\mathbf{g} = -\frac{GM}{r^3}\mathbf{r}$ is the solar gravitational force, $\boldsymbol{\Omega}$ is the solar angular speed and γ is the ratio of specific heats. ρ, $\mathbf{u}$, p, $\mathbf{B}$, $\mathbf{r}$, t, and $\mathbf{g}$ are normalized by the characteristic values ρ_S, a_0, $\rho_S a_0^2$, $\sqrt{\rho_S a_0^2}$, R_S, R_S/a_0, and a_0^2/R_S, where R_S is the solar radius, ρ_S and a_0 are the density and sound speed at the solar surface. The solar rotation is considered in the present study with angular velocity $|\boldsymbol{\Omega}| = 2\pi/26$ radian day^{-1} (here normalized by a_0/R_S). For γ, similar to that of Wu et al. [65], a variable polytropic index is used

$$
\gamma = \begin{cases} 1.05, & r/R_S \le 5 \\ 1.05 + 0.03(r/R_S - 5), & 5 \le r/R_S \le 22 \\ 1.56, & r/R_S > 22. \end{cases}
$$

In the MHD model, we apply the techniques of adding both Powell's source terms $-\nabla \cdot \mathbf{B}(0, \mathbf{B}, \mathbf{v} \cdot \mathbf{B}, \mathbf{v})^T$ [20] and the diffusive control term $\nabla(\nu \nabla \cdot \mathbf{B})$ [29,31,66–68] to deal with the divergence of the magnetic field [66,69,70]. Here, following Feng et al. [29,31], $\nu = 1.3(\frac{1}{\Delta x^2} + \frac{1}{\Delta y^2} + \frac{1}{\Delta z^2})^{-1}$, where Δx, Δy, and Δz are grid spacings in Cartesian coordinates. $\mathbf{S}_m$ and Q_e stand for the momentum and energy source terms, which are responsible for acceleration and heating of the solar wind and are given as follows [15]:

$$
\begin{aligned}
Q_e &= Q_1 \exp\left(-\frac{r}{L_{Q_1}}\right) + Q_2\left(\frac{r}{R_S} - 1\right)\exp\left(-\frac{r}{L_{Q_2}}\right)\\
&\quad + \nabla\left(\xi T^{\frac{5}{2}}\frac{\nabla T \cdot \mathbf{B}}{\mathbf{B}^2}\right) \cdot \mathbf{B},\\
\mathbf{S}_m &= M\left(\frac{r}{R_S} - 1\right)\exp\left(-\frac{r}{L_M}\right)\frac{\mathbf{r}}{r}.
\end{aligned}
\tag{2}
$$

Here, r is the heliocentric distance, Q_1, Q_2 and L_{Q_1}, L_{Q_2} are the intensity and decay height of heating, and T is the temperature, M and L_M are the intensity and the decay height of the momentum addition. A Spitzer type thermal conduction has been added in the third term of Q_e and we choose $\xi = 5\varepsilon_p = 1.6 \times 10^{-12}$ J m^{-1} s^{-1} K$^{-7/2}$ according to Endeve et al. [71]. Here, the constant values of Q_1, Q_0 and M_0 are 1.5×10^{-9} J m^{-3} s^{-1}, 1.18×10^{-7} J m^{-3} s^{-1} and 7.9×10^{-14} N m^{-3}, respectively. L_{Q_1}, L_{Q_2} and L_M are set to be 1 R_S. Here, we assume that $Q_2 = Q_0 C_a$, $M = M_0 C_a$, where $C_a = C_a'/\max(C_a')$ with $C_a' = \frac{\left(5.8 - 1.6e^{[1-(\theta_b/8.5)^3]}\right)^{3.5}}{(1+f_S)^{2/7}}$. The expansion factor [72,73] reads $f_S = \left(\frac{R_S}{R_{SS}}\right)^2 \frac{B_{R_S}}{B_{R_{SS}}}$, where B_{R_S} and $B_{R_{SS}}$ are the radial magnetic field strength at the solar surface and at the solar source surface $R_{SS} = 2.5R_S$. This heating coefficient C_a is a function of two coronal parameters: flux tube expansion factor (f_S), and the minimum angular separation θ_b between an open field foot point and its nearest coronal hole boundary [72,73]. This consideration is motivated by the fact that solar wind speed is inversely related with the expansion factor f_S and that high speed

wind from the center of a coronal hole has large θ_b and low speed wind from the hole boundary has a small θ_b.

The solar wind evolution is calculated in a reference frame of heliographic coordinates corotating with the Sun. For this reference coordinate system we use (r, θ, ϕ) for the position of a point in solar–interplanetary space and (x, y, z) is used to express its corresponding Cartesian coordinates. Sometimes, the analysis of computational results is carried out in the coordinate system at rest to compare with the observations.

3. Cese solver modified space–time conservation element and the solution element method

The mth ($m = 1, 2, \ldots, 8$) equation of the above solar wind MHD equations (1) can be written as:

$$\frac{\partial u_m}{\partial t} + \frac{\partial f_m}{\partial x} + \frac{\partial g_m}{\partial y} + \frac{\partial h_m}{\partial z} (\equiv \nabla \cdot \mathbf{q}_m) = \eta_m \tag{3}$$

where $\mathbf{q}_m = (f_m, g_m, h_m, u_m)$, u_m, f_m, g_m, h_m and η_m are the mth component of $\mathbf{U}$, $\mathbf{F}$, $\mathbf{G}$, $\mathbf{H}$ and η, respectively, and $\mathbf{U}$, $\mathbf{F}$, $\mathbf{G}$, $\mathbf{H}$ and η are solution vector, flux functions in the $x-$, $y-$, $z-$ directions and source terms in Eq. (1). Let (x, y, z, t) be the coordinates of a four-dimensional Euclidean space E_4 and $\nabla = (\partial_x, \partial_y, \partial_z, \partial_t)$ stands for the usual gradient in four dimensional Euclidean space. By using Gauss' divergence theorem in E_4, it can be shown that Eq. (3) is equivalent to the following integral equations:

$$\oint_{S(V)} \mathbf{q}_m \cdot d\mathbf{S} = \int_V \eta_m dV. \tag{4}$$

Here $S(V)$ is the boundary of an arbitrary space–time region V in E_4, and $\mathbf{q}_m \cdot d\mathbf{S}$ is the space–time flux $\mathbf{q}_m$ leaving the region V through the surface element $d\mathbf{S}$. Eq. (4) states that the total space–time flux of $\mathbf{q}_m$ leaving V through its boundary $S(V)$ is equal to the integration of the source term η_m over the space–time region V.

Keep in mind that Powell's source terms $-\nabla \cdot \mathbf{B}(0, \mathbf{B}, \mathbf{u} \cdot \mathbf{B}, \mathbf{u})^T$ and the diffusive control term $\nabla(\nu \nabla \cdot \mathbf{B})$ can be absorbed into the flux terms (f_m, g_m, h_m) and source term η_m as done by Feng et al. [31] without changing the form of Eq. (3). All the arguments of this section and the subsequent sections apply.

Based on the above integral formulation in four dimensional Euclidean space, the space–time conservation element and solution element (CESE) method, has been originally proposed by Chang and co-workers [74–78]. Different substantially from other well-established methods, CESE is not an incremental improvement of a previously existing computational fluid dynamics one. The CESE method's nontraditional characteristics contain a unified treatment of space and time, the introduction of conservation element and solution element, and a novel shock capturing strategy without using Riemann solvers. Note that conservation elements are nonoverlapping space–time subdomains introduced such that (i) the computational domain is the union of these subdomains and (ii) space–time flux conservation can be ensured over each of them and also over the union of any combination of them. In contrast, each solution element is a space–time subdomain, in which any physical flux vector is approximated by using simple smooth functions. Usually, a conservation element does not coincide with a solution element. This method is distinguished by the simplicity of its conceptual basis—a unified treatment of flux conservation in space and time.

It should be noted that one of the most important features of the CESE method is to employ an integral form of space–time flux conservation as the cornerstone for its numerical discretization. However, one derives the conventional finite-volume methods based on Reynolds transport theorem [79], in which space and time are treated separately. By Reynolds transport theorem [79], using Gauss's law in three-dimensional space, the integration form of Eq. (3) can be written as

$$\frac{\partial}{\partial t} \int_{V_{ijk}} u_m dv + \oint_{S(V_{ijk})} (f_m n_x + g_m n_y + h_m n_z) ds = \int_{V_{ijk}} \eta_m dv \tag{5}$$

where dv and ds are the volume and surface element of a fixed spatial control volume V_{ijk} with the centroid indexed by (i, j, k) and $\mathbf{n}$ is a unit vector normal to the surface of the control volume. Alternatively, integrate Eq. (5) with respect to time from t_1 to t_2 to arrive at

$$\int_{V_{ijk}} u_m dv \,|_{t_1}^{t_2} = \int_{t_1}^{t_2} \left(- \oint_{S(V_{ijk})} (f_m n_x + g_m n_y + h_m n_z) ds + \int_{V_{ijk}} \eta_m dv \right). \tag{6}$$

As such, the conservation laws state that the rate of change of the total amount of a substance contained in a fixed spatial control volume V_{ijk} is equal to the combination of the following two factors: (i) the flux of that substance across the boundary $S(V_{ijk})$ of the control volume V_{ijk}, and (ii) the integration of the source term over the fixed spatial domain. The conventional finite volume methods concentrate on the evaluation of the right side of Eq. (6). The left hand side of Eq. (6) is usually discretized by a finite difference method such as the Runge–Kutta methods. Due to the above two factors, the fractional step (or splitting) methods resort to strong measurements of numerically segregating the two factors and treating them in a sequential manner. The numerical fluxes, $(f_m n_x + g_m n_y + h_m n_z)$, at the quadrature point of each face of cell V_{ijk} are determined from the solution of a Riemann problem. Given the left and right inter-face solution states, $\mathbf{U}_L$ and $\mathbf{U}_R$, an upwind numerical flux is evaluated by solving a Riemann problem in the direction defined by the normal to the face. This is, the finite volume method evaluates the change of the conservative values of all control volumes by integrating their interface or edge fluxes. From the point view of programming it consists of two steps, calculating fluxes at every interface and gathering interface fluxes for every control volume. Therefore, the data structure is designed as having two primary arrays, one for control volumes, another for faces, with a bi-directional reference between control volumes and faces.

As pointed out by Zhang et al. [78] and Yu and Chang [80], this separate treatment of space and time prescribes a restriction on the space–time geometry of finite volumes and, as a result, classical Riemann problems arise naturally in the calculation of flux evaluation across an interface. In contrast, due to its unified treatment of space and time, CESE's flux conservation formulation allows a choice of the space–time geometry of CEs that avoids solving Riemann problems. This fundamental difference between the conventional finite-volume methods and the space–time flux conservation formulation unique to the CESE method has been clarified by Zhang et al. [78] Yu and Chang [80].

In what follows we show how to use the CESE method to calculate $\mathbf{U} = (u_1, u_2, \ldots, u_8)$ and its derivatives at a new time level if these values at previous time step are given. The details about the Space–Time CESE method can be found in [78,81,82]. For completeness, a brief discussion of this extended CESE method is provided for hexahedral meshes in spherical shell geometry suitable to solar-terrestrial simulation.

3.1. CEs and SEs in a six-component grid system

In this part, we introduce conservation element and solution element in spherical geometry. Feng et al. [15] propose a composite mesh that consist of six identical component meshes to envelop a

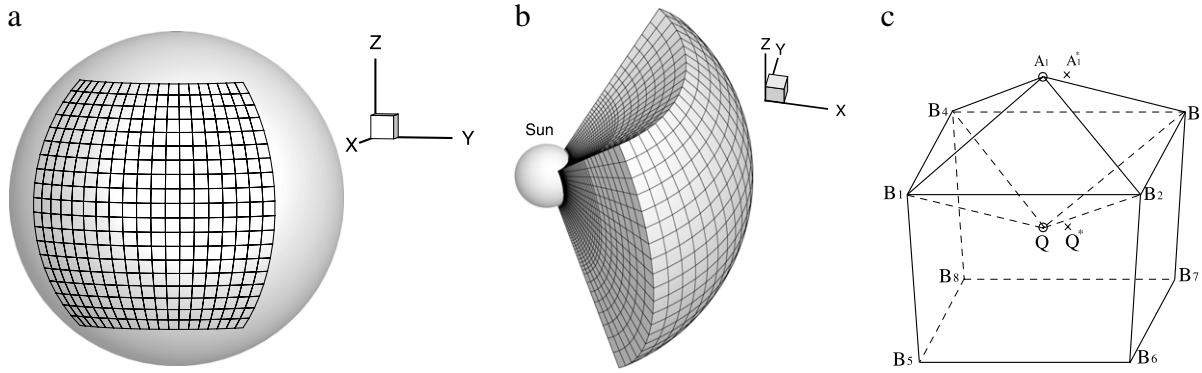

Fig. 1. Grid elements of six-component grid structure for the 3-D CESE solver: (a) one-component grid at solar surface, (b) piling up in the corona, and (c) representative grid cell in the x–y–z space.

spherical surface with partial overlap on their boundaries (Fig. 1). Each component grid is a low latitude spherical mesh, which is defined by

$$\left(\frac{\pi}{4}-\delta\leqslant\theta\leqslant\frac{3\pi}{4}+\delta\right)\cap\left(\frac{3\pi}{4}-\delta\leqslant\phi\leqslant\frac{5\pi}{4}+\delta\right) \tag{7}$$

where δ is determined by the grid spacing and layers of guardcells entailed for the minimum overlapping area of two grid sizes ($\delta = 2\Delta\theta$). Each component is confined by the same region as that in Eq. (7) but in different coordinates. Fig. 1a shows the grid structure on the solar surface or spherical inner boundary. Meanwhile, expand the spherical surface at different radial distances by defining the radial variation. In this paper, we use $r(1) = 1R_S$, $r(i+1) = r(i)+\Delta r(i)$ with $\Delta r(i) = \Delta\theta\times r(i)$. In both θ and ϕ directions, the grid points are even spaced such that $\Delta\theta = \Delta\phi$. In this way, for the r direction, the grid spacing Δr in the r direction is always around $r\Delta\theta$ and $r\sin\theta\Delta\phi$ ($\Delta\theta$ is already chosen to be equal to $\Delta\phi$) so that each grid cell is always approximately a cube. The $\sin\theta$ term varies from 1 to $1/\sqrt{2}$ within the 6 grid components, which shows that avoiding the singularity of the spherical grid indeed results in more regular cells. Then three-dimensional spatial computational domain is divided into non-overlapped convex hexahedrons and any two neighboring hexahedrons share a common surface. Fig. 1b and c show one component of hexahedrons and how to construct a 3-D grid structure by extending the position of spherically allocated grids outward from the inner boundary. For detail of grid structure and grid spacing, one may refer to Feng et al. [15].

After the establishment of 3D spatial grid structure, we are in a position to define conservation element and solution element in space–time domain. Q (marked by a circle) is the centroid of a typical hexahedron $B_1B_2B_3B_4B_5B_6B_7B_8$. Each of the central hexahedron's six neighboring hexahedrons is arbitrarily assigned an identification index $\ell = 1, 2, \ldots, 6$. Also, the centroid of the ℓth neighbor will be denoted by A_ℓ. As an example, the central hexahedron $B_1B_2B_3B_4B_5B_6B_7B_8$ and its 1st neighbor is separated by the quadrilateral $B_1B_2B_3B_4$ in Fig. 1c.

Given any $\ell = 1, 2, \ldots, 6$, a triangle is formed by the point A_ℓ and the two end points of any of the edges of the interface that separates the central hexahedron and its ℓth neighbor. Each of the triangles so formed with the same ℓ is arbitrarily assigned an index $k_\ell = 1, 2, 3, 4$, and denoted by $\triangle(k_\ell, \ell)$. As an example, $\triangle A_1B_1B_2$, $\triangle A_1B_2B_3$, $\triangle A_1B_3B_4$, and $\triangle A_1B_4B_1$ depicted by Fig. 1c have the same $\ell = 1$. Therefore they may be denoted by $\triangle(1, 1)$, $\triangle(2, 1)$, $\triangle(3, 1)$, and $\triangle(4, 1)$ respectively.

Point Q and the two end points (say points B_1 and B_2) of any of the twelve edges of the central hexahedron form a triangle. Each of twelve triangles so formed is arbitrarily assigned an index $j = 1, 2, \ldots, 12$ and denoted by $\triangle(j)$.

The points A_1, B_1, A_2, B_2, A_3, B_3, A_4, B_4, A_5, B_5, A_6, B_6, B_7 and B_8 form a 24-faced polyhedron $B_1B_2B_3B_4B_5B_6B_7B_8A_1A_2A_3A_4A_5A_6$. The centroid of the 24-faced polyhedron is referred to as the solution point associated with point Q. Note that the above 24-faced polyhedron hereafter is denoted by $V(24)$ and the centroid of $V(24)$ is denoted by Q^* and marked by a cross in Fig. 1c.

Given any $\ell = 1, 2, \ldots, 6$, points Q and A_ℓ and the vertices of the quadrilateral interface that separates the central hexahedron and its ℓth neighbor are the vertices of a octahedron. This octahedron hereafter is denoted by $V8(\ell)$. As an example, Q, A_1, B_1, B_2, B_3 and B_4 form a octahedron denoted by $V8(1)$.

In the space–time computational domain, again we assume that $t = n\Delta t$ at the nth time level ($n = 0, \frac{1}{2}, 2, \frac{3}{2}, \ldots$). Also, for a given $n > 0$, let Q, Q', and Q'' (not shown), respectively, be the points on the nth, $(n-\frac{1}{2})$th, and $(n+\frac{1}{2})$th time levels with point Q being their common spatial projection. Other space–time mesh points such as (i) Q'^* and Q''^*, (ii) B_k, B'_k, and B''_k, $k = 1, 2, \ldots, 8$; and (iii) A_ℓ, A^*_ℓ, A'_ℓ, and A'^*_ℓ, $\ell = 1, 2, \ldots, 6$, are defined similarly. Because geometric objects in E_4 generally are difficult to visualize, they will be described analytically in the following discussions.

A "plane" in E_4, by definition, is a subspace of E_4 defined by a linear equation i.e.,

$$a_1x+a_2y+a_3z+a_4t=a_0,\qquad a_1^2+a_2^2+a_3^2+a_4^2\neq 0, \tag{8}$$

where a_k, $k = 0, 1, 2, 3, 4$, are constants. As a result, a hyperplane in E_4 is a three-dimensional subspace. Note that a hyperplane segment, by definition, is a bounded region of a hyperplane. A hyperplane of type I, denoted by $\Gamma(V; t_c)$, is formed by all the points (x, y, z, t) that satisfy the conditions $t = t_c$ and $(x, y, z) \in V$, where t_c is a constant and V denotes a 3D spatial region.

In contrast, a hyperplane segment of type II, denoted by $\Gamma(S; t_-, t_+)$, is formed by all the points (x, y, z, t) that satisfy the conditions $(x, y, z) \in S$ and $t_- \leq t \leq t_+$, where S denotes a spatial plane segment and t_- and $t_+ (t_- < t_+)$ are constants. Note that every point (x, y, z) on the spatial plane segment S satisfies a linear equation of the form

$$c_1x+c_2y+c_3z=c_0,\qquad c_1^2+c_2^2+c_3^2\neq 0,$$

where c_k, $k = 0, 1, 2, 3$, are constants. Thus every point (x, y, z, t) on $\Gamma(S; t_-, t_+)$ also satisfies a special form of Eq. (8).

In addition to the above two types of hyperplanes, we shall also consider "hypercylinder" in E_4. A hypercylinder, denoted by $\Lambda(V; t_-, t_+)$, is formed by all the points (x, y, z, t) that satisfy the conditions $(x, y, z) \in V$ and $t_- \leq t \leq t_+$, where V is a 3D spatial region and t_- and $t_+ (t_- < t_+)$ are constants.

With the above preliminaries, SE(Q^*), the solution element of point Q^*, i.e., the point that lies on the nth time level and has Q^* as its spatial projection, is defined to be the union of $\Gamma(V(24); t^n)$

and $\Gamma(\Delta(j); t^{n-1/2}, t^{n+1/2})$, $j = 1, 2, \ldots, 12$, and their immediate neighborhoods. Moreover, the six Basic Conservation Elements (BCEs) of point Q, denoted by $\mathrm{CE}_\ell(Q)$, $\ell = 1, 2, \cdots, 6$, are defined to be the hypercylinders $\Lambda(V8(\ell); t^{n-1/2}, t^n)$, $\ell = 1, 2, \ldots, 6$, respectively. In addition, the Compound Conservation Element (CCE) of point Q, denoted by $\mathrm{CE}(Q)$, is defined to be $\Lambda(V(24); t^{n-1/2}, t^n)$, i.e., the union of the above six BCEs.

We begin with the following preliminaries:

(a) Let Γ be a hyperplane segment lying within $\mathrm{SE}(Q^*)$. Let A be the area of Γ, (x_c, y_c, z_c, t_c) be the coordinates of the centroid of Γ, and $\mathbf{n}$ be a unit vector normal to Γ. Then it can be shown that

$$\int_\Gamma \mathbf{q}_m^* \cdot d\mathbf{S} = \mathbf{q}_m^*(x_c, y_c, z_c, t_c; Q^*) \cdot A\mathbf{n}$$

where $d\mathbf{S} = d\sigma\mathbf{n}$ with $d\sigma$ being the area of a surface element on Γ. The definition of $\mathbf{q}_m^*(x_c, y_c, z_c, t_c; Q^*)$ is given below.

(b) Let V denote the volume of $V(24)$. Because the unit outward normal vector (outward from the interior of $\mathrm{CE}(Q)$) of this face is $(0, 0, 0, 1)$, its surface vector (i.e., the unit outward normal vector multiplied by the area) is $(0, 0, 0, V)$.

(c) Let V^ℓ and (x^ℓ, y^ℓ, z^ℓ), respectively, denote the volume and the spatial coordinates of the centroid of any $V8(\ell)$. Then the surface vector, and the coordinates of the centroid of $\Gamma(V8(\ell); t^{n-1/2})$, respectively, are $(0, 0, 0, -V^\ell)$ and $(x^\ell, y^\ell, z^\ell, t^{n-1/2})$.

(d) Let $S_{k_\ell}^\ell$, $(n_{k_\ell x}^\ell, n_{k_\ell y}^\ell, n_{k_\ell z}^\ell)$, and $(x_{k_\ell x}^\ell, y_{k_\ell y}^\ell, z_{k_\ell z}^\ell)$, respectively, denote the area, the spatial unit outward normal, and the coordinates of the centroid of any $\triangle(k_\ell, \ell)$. Then the surface vector, and the coordinates of the centroid of the side of face $\Gamma(\triangle(k_\ell, \ell); t^{n-1/2}, t^n)$, respectively, are $(\Delta t/2)S_{k_\ell}^\ell(n_{k_\ell x}^\ell, n_{k_\ell y}^\ell, n_{k_\ell z}^\ell, 0)$ and $(x_{k_\ell}^\ell, y_{k_\ell}^\ell, z_{k_\ell}^\ell, t^n - \Delta t/4)$.

By using the information presented in items (a), (b), (c) and (d), the flux of $\mathbf{q}_m^*$ leaving the other faces of $\mathrm{CE}(Q)$ can be evaluated in terms of the independent marching variables at points $A_\ell'^*$, $\ell = 1, 2, \ldots, 6$.

3.2. Calculation of $(u_m)_{Q^*}$

This subsection is devoted to the calculation of $(u_m)_{Q^*}$ by solving MHD equations on conservation element and solution element defined above. Following Chang's original approach [74], inside each SE the flow variables are assumed smooth, and are represented by the first-order Taylor series. For any $(x, y, z, t) \in \mathrm{SE}(Q^*)$, $u_m(x, y, z, t)$, $f_m(x, y, z, t)$, $g_m(x, y, z, t)$ and $h_m(x, y, z, t)$ are approximated by the following formulae for $u_m^*(x, y, z, t; Q^*)$, $f_m^*(x, y, z, t; Q^*)$, $g_m^*(x, y, z, t; Q^*)$ and $h_m^*(x, y, z, t; Q^*)$:

$$\begin{aligned} u_m^*(x, y, z, t; Q^*) &= (u_m)_{Q^*} + (u_{mx})_{Q^*}(x - x_{Q^*}) \\ &\quad + (u_{my})_{Q^*}(y - y_{Q^*}) \\ &\quad + (u_{mz})_{Q^*}(z - z_{Q^*}) + (u_{mt})_{Q^*}(t - t^n) \end{aligned} \tag{9}$$

$$\begin{aligned} \Gamma_m^*(x, y, z, t; Q^*) &= (\Gamma_m)_{Q^*} + (\Gamma_{mx})_{Q^*}(x - x_{Q^*}) \\ &\quad + (\Gamma_{my})_{Q^*}(y - y_{Q^*}) \\ &\quad + (\Gamma_{mz})_{Q^*}(z - z_{Q^*}) + (\Gamma_{mt})_{Q^*}(t - t^n) \end{aligned} \tag{10}$$

$$u_{m\xi} = \frac{\partial u_m}{\partial \xi}, \qquad \Gamma_{m\xi} = \sum_{\ell=1}^{8} \Gamma_{m\ell}\, u_{\ell\xi}, \quad \Gamma_{m\ell} = \frac{\partial \Gamma_m}{\partial u_\ell}, \tag{11}$$

$$\begin{aligned} q_m^*(x, y, z, t; Q^*) \equiv\ & (f_m^*(x, y, z, t; Q^*), g_m^*(x, y, z, t; Q^*), \\ & h_m^*(x, y, z, t; Q^*), u_m^*(x, y, z, t; Q^*)) \end{aligned} \tag{12}$$

for $m = 1, 2, \ldots, 8$. Here, Γ_m stands for f_m, g_m or h_m, and ξ denotes x, y, z or t. Here, $(\Gamma_{m\ell})_{8\times 8}$ denotes the Jacobian matrix of Γ, which is given in Appendix of Feng et al. [12]. $(x_{Q^*}, y_{Q^*}, z_{Q^*}, t^n)$ is the space–time coordinate of point Q^*. Moreover, we assume that, for any $(x, y, z, t) \in \mathrm{SE}(Q^*)$, and any $m = 1, \ldots, 8$,

$$\begin{aligned} &\frac{\partial u_m^*(x, y, z, t; Q^*)}{\partial t} + \frac{\partial f_m^*(x, y, z, t; Q^*)}{\partial x} \\ &\quad + \frac{\partial g_m^*(x, y, z, t; Q^*)}{\partial y} + \frac{\partial h_m^*(x, y, z, t; Q^*)}{\partial z} = \eta_m. \end{aligned} \tag{13}$$

Obviously, we have

$$\begin{aligned} (u_{mt})_{Q^*} &= (\eta_m)_{Q^*} - (f_{mx})_{Q^*} - (g_{my})_{Q^*} - (h_{mz})_{Q^*} \\ &= (\eta_m)_{Q^*} - \sum_{\ell=1}^{8}[(f_{m\ell})_{Q^*}(u_{\ell x})_{Q^*} \\ &\quad + (g_{m\ell})_{Q^*}(u_{\ell y})_{Q^*} + (h_{m\ell})_{Q^*}(u_{\ell z})_{Q^*}]. \end{aligned} \tag{14}$$

Thus, the space–time flux conservation, Eq. (4), can be approximated by its discrete counterpart on conservation element:

$$\oint_{\mathrm{S(CE)}} \mathbf{q}_m^* \cdot d\mathbf{S} = \int_{\mathrm{CE}} \eta_m dV \tag{15}$$

i.e., the total flux of $\mathbf{q}_m^*$ leaving $\mathrm{CE}(Q)$ through its boundary vanishes. Then, with the aid of the above preliminaries, substituting Eqs. (9) and (14) into Eq. (15), we obtain the following equation

$$(u_m)_{Q^*}^n - \frac{\Delta t}{2}\eta(u_m)_{Q^*}^n = \left(\sum_{\ell=1}^{6} R_m^\ell\right)/V \tag{16}$$

which is the discretized form of the governing equations (3) for the solar wind model. Here

$$\begin{aligned} R_m^\ell &= V^\ell[(u_m)_{A_\ell^*}^{n-1/2} + (x^\ell - x_{A_\ell^*})(u_{mx})_{A_\ell^*}^{n-1/2} \\ &\quad + (y^\ell - y_{A_\ell^*})(u_{my})_{A_\ell^*}^{n-1/2} + (z^\ell - z_{A_\ell^*})(u_{mz})_{A_\ell^*}^{n-1/2}] \\ &\quad - \frac{\Delta t}{2}\sum_{k_\ell=1}^{4} S_{k_\ell}^\ell \Big\{ n_{k_\ell x}^\ell[(f_m)_{A_\ell^*}^{n-1/2} + (x_{k_\ell}^\ell - x_{A_\ell^*})(f_{mx})_{A_\ell^*}^{n-1/2} \\ &\quad + \frac{\Delta t}{4}(f_{mt})_{A_\ell^*}^{n-1/2} + (y_{k_\ell}^\ell - y_{A_\ell^*})(f_{my})_{A_\ell^*}^{n-1/2} \\ &\quad + (z_{k_\ell}^\ell - z_{A_\ell^*})(f_{mz})_{A_\ell^*}^{n-1/2}] \Big\} \\ &\quad - \frac{\Delta t}{2}\sum_{k_\ell=1}^{4} S_{k_\ell}^\ell \Big\{ n_{k_\ell y}^\ell[(g_m)_{A_\ell^*}^{n-1/2} + (x_{k_\ell}^\ell - x_{A_\ell^*})(g_{mx})_{A_\ell^*}^{n-1/2} \\ &\quad + \frac{\Delta t}{4}(g_{mt})_{A_\ell^*}^{n-1/2} + (y_{k_\ell}^\ell - y_{A_\ell^*})(g_{my})_{A_\ell^*}^{n-1/2} \\ &\quad + (z_{k_\ell}^\ell - z_{A_\ell^*})(g_{mz})_{A_\ell^*}^{n-1/2}] \Big\} \\ &\quad - \frac{\Delta t}{2}\sum_{k_\ell=1}^{4} S_{k_\ell}^\ell \Big\{ n_{k_\ell z}^\ell[(h_m)_{A_\ell^*}^{n-1/2} + (x_{k_\ell}^\ell - x_{A_\ell^*})(h_{mx})_{A_\ell^*}^{n-1/2} \\ &\quad + \frac{\Delta t}{4}(h_{mt})_{A_\ell^*}^{n-1/2} + (y_{k_\ell}^\ell - y_{A_\ell^*})(h_{my})_{A_\ell^*}^{n-1/2} \\ &\quad + (z_{k_\ell}^\ell - z_{A_\ell^*})(h_{mz})_{A_\ell^*}^{n-1/2}] \Big\} \end{aligned} \tag{17}$$

where $\ell = 1, 2, \ldots, 6$, for flux conservation contributed from six neighboring CEs. Using the Eqs. (16) and (17) given above, it can be seen clearly that, for the current 3D case, the only independent discrete variables associated with the space–time solution point Q^* are $(u_m)_{Q^*}$, $(u_{mx})_{Q^*}$, $(u_{my})_{Q^*}$, $(u_{mz})_{Q^*}$, $m = 1, \ldots, 8$. We can see that at time step $n-1/2$ if the solution variables $(\mathbf{U})_{A_\ell^*}^{n-1/2}$ and their first-order spatial derivatives $\left((\mathbf{U}_x)_{A_\ell^*}^{n-1/2}, (\mathbf{U}_y)_{A_\ell^*}^{n-1/2}, (\mathbf{U}_z)_{A_\ell^*}^{n-1/2}\right)$

are known, the solution variables $\mathbf{U}^n_{Q^*}$ at the nth time step can be obtained by solving Eq. (16) with Newtonian solvers [12,15].

In order to accomplish the CESE solver, we have to update the solution variables' gradients U_{mx}, U_{my} and U_{mz} on a solution point Q^*, which are obtained by using a reweighting scheme [12,15,78].

In order to realistically generate the structured solar wind, we specify the inner initial boundary magnetic field with the observed line of sight photospheric magnetic field data. The observed photospheric magnetic field from the Wilcox Solar Observatory (WSO) at Stanford University is used to deduce a 3-D global potential magnetic field as initial magnetic input. Parker's solar wind flow provides the initial distributions of the plasma density ρ, gas pressure p, and the plasma velocity $\mathbf{u}$. Here, the initial solar surface temperature and number density are set to be 1.3×10^6 K and 1.5×10^8 cm^{-3}, respectively. Then, our code is run in time-relaxation manner until a steady-state equilibrium between flow and magnetic fields is achieved by satisfying some error criteria [12].

The calculations are performed between $1\,R_S$ (i.e., the base of the corona) and $328\,R_S$. At the lower boundary, basing on the observed line-of-sight measurements of the photospheric magnetic field from Wilcox Solar Observatory (WSO) at Stanford University, we specify the radial component of the magnetic field. The initial solar surface temperature and number density are set to be 1.3×10^6 K and 2.0×10^8 cm^{-3}, respectively. We employ the time-dependent inner boundary condition to limit the mass flux escaping through the solar surface and adjust the distribution of temperature, number density and speed on the solar surface [15,34,83]. Then, the code is initialized by using potential magnetic field based on the line-of-sight measurements of the photospheric magnetic field for the CRs of interest and Parker solar wind solution. Finally, our model is run in time-relaxation method until a dynamic, steady-state equilibrium is achieved. In fact, the same procedure of boundary conditions and initial conditions given in Section 6 of Feng et al. [15] is used in the present paper.

4. Block-structured hexahedral adaptive mesh refinement

In this article, we carry out our AMR implementation with the help of PARAMESH publicly available at http://sourceforge.net/projects/paramesh/, which is a package designed to ease the task of adding parallelization and dynamic, adaptive mesh refinement (AMR) [84]. Previously we have implemented the adaptive mesh refinement (AMR) implementation of SIP-CESE MHD model [12,15,31] under six-component grid system, with the aid of PARAMESH through a curvilinear coordinate transformation. Here, instead of using the coordinate transformation we employ a solution-adaptive technique proposed by Sun and Takayama [85]. A hexahedral grid structure for three dimensions has been established by Sun and Takayama [85], where every cell points to its six faces, and every face points to its two neighboring cells, as shown in Fig. 2. Every face is uniquely oriented such that its two neighboring cells can be identified by *left* and *right*, according to the orientation as shown in Fig. 2b. The six faces of each cell are ordered by the following rules: 1) the same orientation must be assigned to two opposite faces; 2) the orientations of three pairs of opposite faces must constitute a local right-handed coordinate frame in which six faces is unambiguously ordered. These definitions and neighboring information are sufficient to be required by establishing the CESE solver in Eqs. (16) and (17).

As pointed out by Sun and Takayama [85], these strict definitions in the data structure reduce the complexity of the unstructured adaptive solver without losing generality, and do not require additional memory to store the definitions, but store the neighboring cell information following the rules.

In the AMR strategy [84,86], a subgrid will be created in regions of its parent grid needing higher resolution, and each grid evolves as a separate initial boundary value problem. The whole grid hierarchy evolves recursively, and organized in a tree structure. As usual, in the refinement procedure, the one-level-difference rule that no two neighboring cells differ by more than one refinement level is obeyed. That is, once a cell cannot be refined due to the level difference between itself and one or a few neighboring cells, the neighboring cells are refined no matter what values of their refine and coarse are. A cell to be refined is divided into eight children as shown in Fig. 2c.

The physical values at newly generated cells in the adaptation procedure are determined by those on the old mesh according to the method proposed by Sun and Takayama [85]. That is, in the refinement procedure the conservative variables of new children are linearly interpolated from those of their parent, while in coarsening procedure flow variables of a coarsened parent cell are the volume-weighted average of these of its deleted children. This kind of interpolation and the weighted average for new cells has been proven to preserve conservation [87].

With the above orientation or ordering of cells and interpolation during the refining and coarsening process, PARAMESH can be easily accommodated to manage our AMR grid system such that we can directly use most of the default operations provided by PARAMESH, such as the refining or coarsening of the blocks, prolongation, and restriction. Therefore, the data transferring and guard cell filling between blocks can be automatically accomplished by the PARAMESH package without large modification. However, the ghost cell filling of the edges of each of the six components is achieved as follows. On the overlapping area between two components, solution values at the ghost cell centers of one component grid are determined by the standard Lagrange interpolation from its neighboring component. The grid layer buffer δ is suitably chosen for the overlapping region to perform such interpolation. In this paper, $\delta = 2\Delta\theta$ is chosen such that the overlapping region between two components contains at least two layers of grid cells of each other to guarantee that none of the neighboring component's ghostcell centers is used in the interpolation stencil. For instance, a ghost cell center G has coordinates (x_G, y_G, z_G) in its corresponding neighboring component, which does not necessarily coincide with any mesh cell center of the neighboring component, while the ghost cell center G's coordinates can be denoted by (x'_G, y'_G, z'_G) when seen as a point in the ghostcell associated component. The interpolated value u_m at the point $G(x_G, y_G, z_G)$ in the neighboring component is computed by $u_m(G) = \sum_{k=0}^{2}\sum_{j=0}^{2}\sum_{i=0}^{2} P_i^G(x)P_j^G(y)P_k^G(z)u_m(x_i, y_j, z_k)$, where $P_l^G(\xi)$ is the Lagrange interpolating polynomial $P_l^G(\xi) = \prod_{k=0,k\neq l}^{2} \frac{\xi_G-\xi_k}{\xi_l-\xi_k}$ with ξ being x, y or z and u_m the mth component of the solution vector $\mathbf{U}$. The twenty-seven (3^3) nodes with coordinates (x_i, y_j, z_k) $(i, j, k = 0, 1, 2)$ denote the inner mesh cell centers of the very neighboring component that are closest to G, and these values $u_m(x_i, y_j, z_k)$ $(i, j, k = 0, 1, 2)$ are already known in the neighboring component. Afterwards, through the transformation between components, $\mathbf{U}(G) = (u_1(G), \ldots, u_8(G))$ at the point $G(x_G, y_G, z_G)$ is converted to $\mathbf{U}'(x'_G, y'_G, z'_G)$ in the ghostcell associated component, and $\mathbf{U}'(x'_G, y'_G, z'_G)$ is used to fill the value at the ghost cell center $G(x'_G, y'_G, z'_G)$. The transformation of velocity and magnetic field vectors in the solution vector $\mathbf{U}$ between different components has been provided in detail by [15]. This kind of interpolation with the third order accuracy works well in practice [29,31,60] for our second order accurate CESE solver.

Initially, the computational domain in every component is divided into $14 \times 4 \times 4$ blocks with each block consisting of $8 \times 8 \times 8$ cells with one layer of guardcell included. These correspond to $N_\theta = N_\phi = 25$ and $\Delta\theta = \pi/48$ by defining grid points on

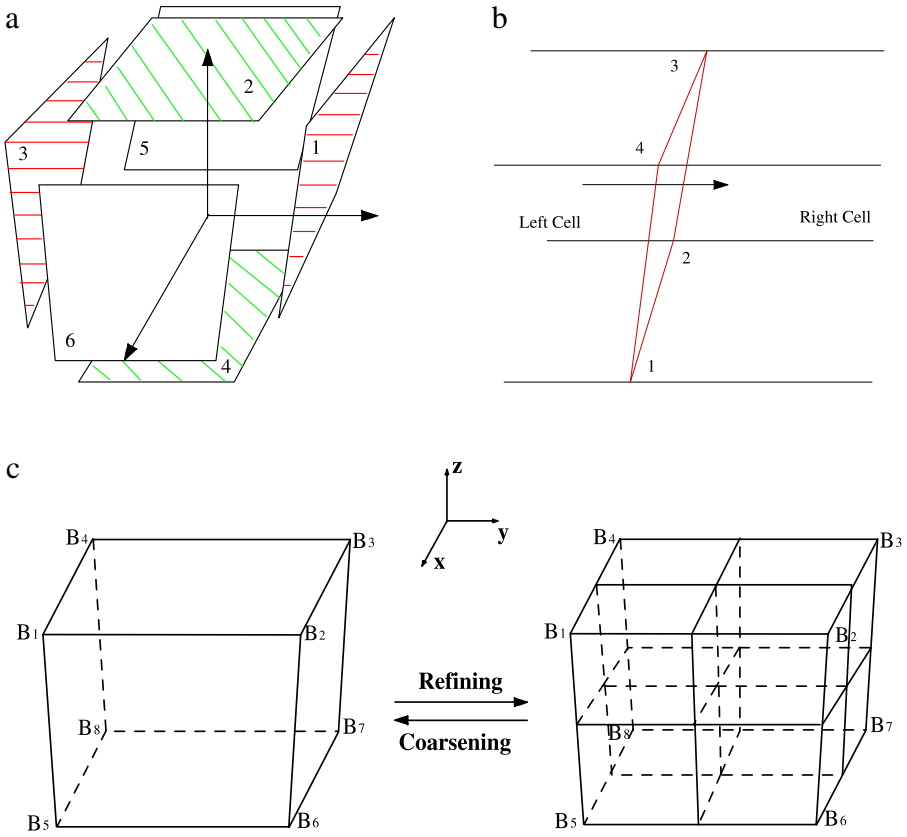

Fig. 2. AMR strategy for grid adaptation: (a) every cell stores its location and points to six faces; (b) every face stores the locations of its four vertices and points to two neighboring cells; and (c) a parent cell is divided into eight children.
Source: Adopted from Sun and Takayama [85].

each component in physical space as $\theta_j^\ell = \theta_{\min} + j\Delta\theta, j = 0, 1, \ldots, N_\theta + 1, \phi_k^\ell = \phi_{\min} + k\Delta\phi, k = 0, 1, \ldots, N_\phi + 1$ and $\Delta\theta = (\theta_{\max} - \theta_{\min})/(N_\theta - 1)$, $\Delta\phi = (\phi_{\max} - \phi_{\min})/(N_\phi - 1)$, where N_θ and N_ϕ are the mesh numbers of the latitude and longitude, respectively. $\theta_{\min} = \frac{\pi}{4}, \theta_{\max} = \frac{3\pi}{4}, \phi_{\min} = \frac{3\pi}{4}, \phi_{\max} = \frac{5\pi}{4}$. The innermost region is set on the solar surface at 1 R_S and the outermost region on the sphere at 328 R_S.

Here, all the ranks are classified into six groups, each of which corresponds to one component grid system and deals with the same kind of grids, basic equations, and numerical task. The block size is set to be $8 \times 8 \times 8$ cells, with one layer of guard cells included. Due to the importance of the topology of heliospheric current sheet, only the curl of the magnetic field is used as our refinement strategy to capture the current sheet. We strictly follow Feng et al. [31] by setting the thresholds of refining and coarsening criterion according to different physical time intervals during the code's running. Under this setting, a grid cell size of 0.015 R_S on the solar surface is achieved through three levels of grid refinement. The grid cell size is about 0.15 R_S near the current sheet within 20 R_S and about 0.7 R_S near 1 AU. At the same time, the maximum grid cell size is 1.3 R_S in the corona and 7 R_S in the inner heliosphere. Furthermore, a multiple time-stepping algorithm is implemented with the radial direction decomposed into six subdomains: 1–10 R_S, 10–20 R_S, 20–50 R_S, 50–100 R_S, 100–170 R_S, 170–328 R_S. For details see Feng et al. [31].

5. Positivity-preserving consideration in the SIP-CESE MHD model

Positivity-preservation is a crucial property that a flux discretization scheme should possess. Positivity-preservation stands for the capability to preserve the positivity of the determinative properties for the solution to be positive within physically-permitted bounds. In ideal MHD, density ρ and pressure p should be non-negative, but such positivity property is not always satisfied by approximated solutions. One can encounter this when simulating problems with low density, high Mach number, or much large magnetic energy compared with internal energy. When this occurs, numerical instability may develop and the simulation can break down. Therefore, a method guaranteeing positivity of the determinative properties has to be considered in a numerical design.

When the MHD equations are written in near conservative form, in order to derive the value of the pressure p one has to subtract off the kinetic energy $\frac{1}{2}\rho\mathbf{u}^2$ and magnetic energy $\frac{\mathbf{B}^2}{2}$ from the total energy $e = \frac{1}{2}\rho\mathbf{u}^2 + \frac{p}{\gamma-1} + \frac{\mathbf{B}^2}{2}$, which can be quite large relative to the value of the internal energy or pressure, especially in regions such as the solar corona with very small plasma $\beta = \frac{2p}{\mathbf{B}^2}$. Such case can lead to positivity problems (that ensures that density and pressure remains positive in a scheme under a suitable CFL-condition) (e.g., Gombosi et al. [36], Janhunen [41], Balsara and Spicer [88], Waagan [89], Fuchs et al. [90]). Thus discretization errors made in computing the total energy and the kinetic energy and magnetic energies can be large enough to generate negative pressure. This results in an unacceptable physical situation in the computation of solar-terrestrial space plasma flows.

In order to maintain pressure positivity, Balsara and Spicer [88] used a hybrid scheme: both the conservative energy and the entropy equations are solved. Close to shock waves the energy equation is used to obtain the correct weak solution, at other places the more robust and positive entropy equation $\frac{\partial}{\partial t}\left(\frac{p}{\rho^{\gamma-1}}\right) + \nabla \cdot \left(\mathbf{u}\frac{p}{\rho^{\gamma-1}}\right) = 0$ can be used. That is, the conservative energy and

entropy equations are switched to be solved according to some criteria of shock identifier. Similarly, instead of entropy equation, in regions of small plasma β and/or dynamic pressure, the pressure equation $\frac{\partial p}{\partial t} + \nabla \cdot (\mathbf{u}p) = -(\gamma - 1)p\nabla \cdot \mathbf{u}$ is used to replace the conservative energy equation [8,15]. That is, instead of solving the total energy equation we use the internal energy $\varepsilon = \frac{p}{\gamma - 1}$ equation

$$\frac{\partial \varepsilon}{\partial t} + \nabla \cdot (\varepsilon \mathbf{u}) = -p\nabla \cdot \mathbf{u} + Q_e \tag{18}$$

in those unsafe regions such as $\beta < 0.01$ or $\varepsilon/e_1 < 0.05$.

In MPI-AMRVAC (Message-Passing Interface-Adaptive Mesh Refinement Versatile Advection Code), Keppens et al. [68] suggested a positivity fixing strategy as follows: identify all cells (within the same grid block) that represent physical states surrounding a faulty cell in a rectangular zone up to n_{pos} cells away; (2) convert those cells to primitive variables; and (3) for all but the magnetic field components, replace the faulty cell values by the average of surrounding physical state cells. Finally, conservative variables are reverted where needed.

It is helpful in positivity fix to use the splitting method by writing the full magnetic field vector $\mathbf{B}$ as the sum of a time-independent potential magnetic field $\mathbf{B}_0$ and a deviation $\mathbf{B}_1$ (i.e., $\mathbf{B} = \mathbf{B}_0 + \mathbf{B}_1$), where $\mathbf{B}_1$ is calculated by the numerical scheme. After splitting, this problem can be mitigated by rewriting the energy equation in terms of the modified total energy density

$$e_1 = \frac{1}{2}\rho\mathbf{u}^2 + \frac{p}{\gamma - 1} + \frac{1}{2}\mathbf{B}_1^2. \tag{19}$$

As pointed out by Gombosi et al. [36], solving for the deviation $\mathbf{B}_1$ from the embedded field $\mathbf{B}_0$ is inherently more accurate than solving for the full magnetic field vector $\mathbf{B}$. This splitting approach was first suggested by Ogino and Walker [91], applied to the Godunov-type schemes by Tanaka [17] and Nakamizo et al. [13], the Roe-type approximate Riemann solver by Powell et al. [20] and Gombosi et al. [36], and the CESE scheme employed by Feng et al. [15,29,31].

For other useful techniques in positivity-preserving, please refer to the recent works by [92,93].

In the present paper, we employ the following switches: first solve Eq. (3); Second, if negative values occur, switch to solve Eq. (18); Third, if there still exist negative values, switch to the positivity fixing strategy proposed by Keppens et al. [68] and finally rederive the total energy from Eq. (19). In the solar wind modeling, the radial speed should be kept to flow out. That is, v_r must be positive. The non-positiveness of v_r may occur in the near solar surface. In order to confirm the positiveness of v_r during the calculation, we also replace the faulty cell values by the average of surrounding physical state cells.

6. Considerations of a second order accuracy AMR scheme

Sufficient spatial resolution is one desirable characteristic for a numerical discretization scheme. It involves the capability to capture with few nodes continuous and discontinuous waves while not introducing spurious oscillations, and can be usually achieved through flux or slope limiters in a numerical scheme. High-order resolution approximations more than second order (for instance, the piecewise parabolic method (PPM) [94,95] or corner transport upwind PPM (CTU-PPM) [96,97] or 5th order weighted essentially non-oscillatory (WENO) [98] are effective in increasing the accuracy per unit mesh cell of finite difference methods under almost all circumstances. This also appears to be true for flows containing discontinuities such as shock waves. The nature of their effectiveness must include the increased cost incurred when invoking higher order approximations. The general belief is that the high-order numerical scheme will provide greater accuracy although the high-order method is complex and time consuming. The question to be considered is whether such improvement in accuracy is worth the additional cost. By taking account of the "balance" between accuracy and cost, we suggest that the MHD modeling from the Sun to Earth benefits from the second order scheme. In particular, in numerical study of solar-terrestrial physics problems, we prefer the AMR implementation of the 2nd order spatial resolution scheme without flux vector splitting. Here are given our comments on the advantages of using such kind of schemes.

On one hand, since formal order of accuracy is lost in a shock wave propagating in a coupled system of equations [99], the higher order methods do not accumulate the significant advantage available for smooth linear problems. In coupled hyperbolic problems with discontinuities, it was proven by Majda and Osher [99] that numerical methods with modest restrictions are subject to a loss of formal accuracy. The accuracy degenerates to first-order in all, but very special cases between characteristics emanating from a discontinuity. Later work [100,101] has revisited this issue, but without any evidence to modify Majda and Osher's result. Examples are found by Donat and Osher [100], where sub-cell resolution can overcome this problem. To some extent, in analogy, this problem can be reduced or mitigated by the AMR scheme because of the ability of the scheme to place grid points at the location in the flow where the largest truncation errors occur [86].

Greenough and Rider [102] and Rider and Kamm [103] carried out a quantitative comparison of numerical methods for the compressible Euler equations: fifth-order WENO, The piecewise parabolic method (PPM) and piecewise-linear method (PLM) of Godunov. In light of their conclusions, the higher-order method's advantage observed in the linear regime is not pronounced when nonlinearity is introduced. Similar work in this area indicates that the multi-dimensional results share similar phenomena that formally high order methods are comparable to the second-order Godunov method for nonlinear problems in multiple spatial dimensions [A.W. Cook, W.H. Cabot, J.A. Greenough, A comparison of high and low order schemes for shock-induced mixing, UCRL-JC-144109.]. These studies show that the impact of the grid spacing is more important than that of the difference accuracy on the performance of a numerical scheme.

On the other hand, the governing equations describing the solar wind plasma are often modified to include other terms such as the thermal conduction and the resistivity, divergence—cleaning procedure, which leads to the difficulty in globally guaranteeing the same high-order accuracy as the high-order scheme owns. As done in the numerical study of incompressible Navier–Stokes equations, simulations of turbulent channel flow indicate that the second-order central-difference scheme resolves the turbulent spectrum better than the high-order upwind schemes, and there is little evidence that the high-order treatment of the pressure equation adds sufficiently to the overall accuracy of the scheme even if fourth-order accurate central-difference approximations are used to construct high-order Laplacians in the pressure equation [104]. Also, AMR reflux and interpolation method may mitigate the overall high-order accuracy. Usually, higher-resolution numerical schemes need more ghostcells, which must be taken care of in AMR implementation in order to keep flux conservation. In particular, more ghostcells bring the challenging of the inner boundary determination at the solar surface [15]. So far, efforts to achieve better accuracy in numerical relativity have focused either on implementing second order accurate adaptive mesh refinement or on defining higher order accurate differences and update schemes. Lehner et al. [105] argued for the combination that adaptive gridding techniques provide to resolve fine scales (in addition

to a more efficient use of resources) together with the higher accuracy furnished by higher order schemes when the solution is adequately resolved. But, to define a convenient higher order adaptive mesh refinement scheme should devise a novel approach to dealing with the grid boundaries for the use of high order operators within an adaptive framework.

Although many higher order accurate schemes such as WENO and PPM have existed for a long time, implementing them to the AMR framework is still in its infancy. Li and Hyman [106] combined high order finite difference WENO with AMR, where the use of a piecewise linear prolongation in space reduces the scheme to second order accuracy. Shen et al. [107] proposed a finite difference AMR-WENO method for hyperbolic conservation laws by combining the AMR framework with the high order finite difference WENO method in space and the total variation diminishing (TVD) Runge–Kutta (RK) method in time (WENO-RK) by a high order coupling. These WENO-AMR studies showed a significant improvement of the fifth order AMR-WENO over the third order one, not only in accuracy for smooth problems, but also in its ability in resolving complicated solution structures, due to the very low numerical diffusion of high order schemes. At the same time, it is found that designing a robust AMR-WENO scheme that is both conservative and high order (higher than second order) is a difficult task, due to the mass inconsistency of coarse and fine grid solutions at the initial stage in a finite difference scheme. In realizing such high order coupling, the following major roadblocks exist: 1) it is difficult to maintain high order accuracy across several levels of grids. In the AMR algorithm, the fine mesh solutions are interpolated from the coarse mesh solutions. Solutions at boundary points are needed not only at the current time but also at intermediate fine grid time steps (subcycles) as well as RK sub-stages. The same temporal and spatial accuracy are required in the data prolongation procedures as those of the base integrator. 2) introducing a high order accurate scheme in the AMR setting makes it harder to maintain local mass conservation. It is critical to conserve the properties of solutions when the mesh resolution changes. According to Berger and Colella [86], a flux correction step was introduced to preserve the mass conservation for the traditional finite volume AMR method. However, the space–time conservative CESE formulation differs from previous techniques because of global and local flux conservation in a space–time domain without resorting to interpolation or extrapolation, and no flux correction was needed [74,75]. 3) in a higher order accurate scheme, robust and inexpensive refinement criteria are difficult to find. 4) For the MHD equations, multi-dimensional AMR MHD computations must handle the additional complication of maintaining a solenoidal magnetic field [8,29,31,68]. Although Berger and Colella [86] proposed an adaptive mesh refinement (AMR) scheme for hydrodynamics to conserve scalar quantities (e.g., mass, energy) and numerical fluxes, additional challenges are presented in physical systems satisfying the Stokes's law type of equation with the divergence free evolution of vector fields, such as velocity fields in incompressible hydrodynamics and magnetic fields in magnetohydrodynamics (MHD). Divergence control methods are highly application dependent. As pointed out by Tóth et al. [8], since the $\nabla \cdot \mathbf{B} = 0$ condition is a consequence of the initial condition only, the local time stepping conventionally used in AMR will lead to a steady state solution with non-zero $\nabla \cdot \mathbf{B}$, if nothing is done for the modification of the induction equation (such as the 8-wave scheme [20], the parabolic/hyperbolic cleaning or the generalized Lagrangian multiplier [108], and the projection scheme [109] so that the divergence free condition depends on the boundary conditions and not on the initial conditions. And the constrained transport scheme [110–112], although popular, cannot be combined with the local time stepping towards steady state, because it relies on the initial condition to maintain the divergence-free magnetic field. Meanwhile, although the directionally splitting approach can be easily applied to any kind of grids and in any dimensions for hydrodynamic problems, it is unsuitable for MHD in that dimensionally split MHD algorithms cannot preserve the divergence-free constraint between each one-dimensional update [96,97,113], because it is impossible to enforce the divergence-free constraint between partial updates unless all three components of the magnetic field are updated together, which in turn violates the assumption crucial to the splitting method that each dimensional operator is independent and can be split from the others. As pointed out by Balsara [113], the directionally split algorithms are also unsuitable for AMR applications in which the fluxes and electric fields that are needed for flux correction or electric field correction steps should contain all the contributions from all the waves that arrive at the boundaries or the edges (e.g., Balsara [114–116]). In principle, the fluxes and fields that are obtained from directionally split algorithms do lose this property, while the unsplit algorithms do have this attribute. Although the CESE method does not inherently satisfy the discrete divergence constraint of the magnetic field, the numerical results from the application of the CESE method cannot be improved further by using a divergence cleaning procedure [8,15,29,31,117–121] such as the projection method, the constraint-transport method, the hyperbolic/parabolic cleaning method or the generalized Lagrangian multiplier, and eight-wave method.

A detailed comparison of AMR versus high order schemes is given by Jameson [122] for a range of different problems. It is believed that the AMR scheme will be advantageous if the AMR region is below a certain proportion of the entire domain; and that it is advantageous to have an AMR scheme with as high order as the regularity of the partial differential equation. As pointed out by Jameson [122], AMR methods can be very effective as long as two fundamental requirements are satisfied: (1) The region of the domain needing refinement must be confined to a relatively small fraction of the computation domain. Roughly no more than 1/3 of the domain should be at the finest grid spacing. (2) The numerical order of the AMR scheme should be as close as possible to the numerical order of the computational data and should not exceed it. That is, if one has a flow that is essentially shock dominated, roughly of piecewise linear structure, and if the shocks never fill more than 1/3 of the domain, then low order AMR schemes can offer a large computational savings when compared to other methods of calculation. These two fundamental requirements are evidenced by the solar-terrestrial phenomena such as heliospheric current sheet (HCS), corotating interaction regions (CIRs) and coronal mass ejections (CMEs) or interplanetary shocks, which can never occupy more than 1/3 of the vast solar-terrestrial space.

The last but not the least point we want to mention is that the degeneracy of eigenvalues in MHD system suggest us to avoid the flux-splitting schemes as possible as we can. The MHD equation system forms a non-strictly hyperbolic system. The eigenvalues also can reduce locally to coincide with each other when the magnetic field switches polarity. As a consequence, the analytic structure of the weak solution is unknown where degeneracy occurs. Nevertheless, most numerical approaches for solving this equation system adopt the characteristic-based or approximate Riemann [123–125] and total variation diminishing (TVD) schemes [17].

The basic idea of the characteristic-based methods, either the flux vector splitting or flux difference splitting (often referred to as the approximate Riemann or Godunov approach) for identifying upwind directions in solving a hyperbolic equation system, is derived from eigenvalue and eigenvector analysis [126,127]. A distinguishing feature of upwind numerical methods is that the discretization of the equations on a mesh is performed according to the direction of propagation of information on that mesh. The essential process in numerical scheme designs is to construct a non-singular similarity matrix and its left-hand inverse from

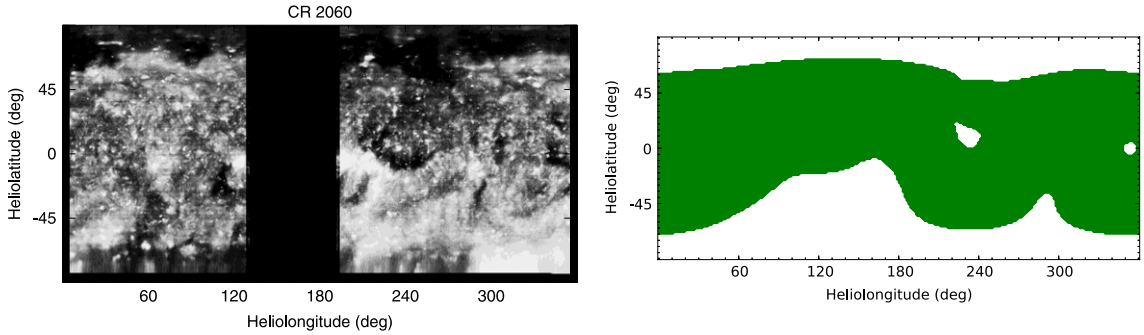

Fig. 3. Synoptic maps of the coronal holes at 1 R_S for CR 2060. The left panel is the SOHO/EIT 195 Å observation, in which the black vertical stripes represent data gaps. The right one presents the open-field regions and closed-field ones from the SIP-AMR-CESE MHD model, where the green shaded areas are of closed magnetic field and the white regions are of open field. (For interpretation of the references to colour in this figure legend, the reader is referred to the web version of this article.)

the eigenvectors of the coefficient matrices in each spatiotemporal dimension. Through this process, the formulation reduces to the Riemann, or at the least, the approximate Riemann problem [126]. Many flux difference splitting methods of Godunov type for MHD system have been designed such as HLL (Harten–Lax–van Leer)-type schemes [41,42,112,128–132]. The flux vector splitting methods are developed by MacCormack [133] and Jiang and Wu [98]. The MHD equations are not homogeneous of degree one with respect to the state vector and hence cannot directly perform flux vector splitting. To overcome this numerical difficulty, Powell et al. [20,123] successfully imposed Gauss's law as a modifier to the Jacobian coefficient matrices. Also, MacCormack [133] demonstrated that the flux vectors could be expanded to preserve the homogeneous of degree one property for the MHD equations. He has found a Jacobian matrix that leads to the identical eigenvalues and eigenvectors derived by Powell et al. [20]. Their efforts have paved the way for applying a characteristic-based scheme for computational MHD. In characteristic-based methods, all the flux-splitting schemes prove to be dissipative [134] and very recently a method of reducing numerical diffusion in some characteristic-based methods is proposed by Tóth et al. [135]. In order to reduce the numerical dissipation, Yee and Sjögreen [136] designed a class of low dissipative high order (fourth or higher-order Lax–Friedrichs scheme or an approximate Riemann solver) filter schemes for MHD systems with the minimization of the divergence of the magnetic field $\nabla \cdot \mathbf{B}$ numerical error but without having to deal with an incomplete eigensystem set while at the same time ensuring that correct shock speeds and locations are computed in the ideal conservative MHD system. As noted by Shen et al. [137], in the eigensystem of Roe and Balsara [138] and Cargo and Gallice [139], the eigenvalues of the Alfvén waves have no affect on the flux. In other words, any values can be used for the eigenvalues of the Alfvén waves and the flux will be the same. This makes the flux splitting based on Roe's approximate Riemann solver uncertain. Another kind of low diffusion higher order schemes for MHD system [137,140] was developed by combining the convective upwind and split pressure (CUSP) WENO scheme with the constrained transport algorithm. This scheme simultaneously considers the convective upwind characteristics and avoids the complication of deriving the eigenvalues and eigenvector system when the MHD equations are incorporated. These kinds of low dissipative schemes may be helpful in mitigating the numerical dissipation of future consideration in solar wind modeling but presently they are usually of higher order spatial accuracy.

Roe [126] has pointed out that one could not expect to find a legitimate solution by solving differential equations in regions where the true solution is not differentiable. Therefore, the numerical methods built on the integral rather than differential conservative laws should be preferentially considered. In the CESE method, by treating space and time as one entity, the ideal MHD equations are formulated in a space–time integral form, and are solved by the space–time conservation element and solution element method. Contrast to the modern upwind methods, no reconstruction procedure or Riemann solver is needed in this approach. Its computational logic and operational count are much simpler and more efficient. Moreover, no special treatment has been employed to maintain the divergence-free condition for the magnetic field [118,119]. Nevertheless, the divergence free constraint has been faithfully maintained in smooth region, while the magnitude of $|\nabla \cdot \mathbf{B}|$ is bounded in regions near shocks.

Near the computational domain boundaries, the accuracy of the spatial derivatives has to be decreased. Conventionally, centered differences have to be replaced by one-sided differences because grid points are available only on the interior side of the boundary. As pointed out by Poinsot and Lele [141], the overall accuracy of the scheme is not affected if the order of approximation near the boundary is equal to the scheme order minus one. Numerical validations [15,29,55,58,60] indicate that this is not a major difficulty.

Based on the above arguments or comments, we prefer to use the 2nd order spatial resolution schemes in solar wind modeling. To some extent, based on the space–time conservation integral method without using Riemann solver, the CESE MHD solver of second order accuracy in space–time domain is one of the best candidates for MHD-based modeling solar-terrestrial physics problems.

7. Numerical results

In this section, we concisely present the model's results for the steady solar corona and interplanetary space in CR 2060 and compare them with the observations from multiple spacecraft to validate the performance of the SIP-CESE MHD model with AMR of hexahedral meshes developed in the previous sections. In fact, the solar wind background in the inner heliosphere during CR 2060 has been investigated by some researchers [28,31,58,142], and here we select it as our studied interval in order to better assess the model.

7.1. Steady corona

One of the most striking features of the large-scale solar corona is coronal holes, which are believed to be associated with open magnetic field regions and to be the source regions of fast solar wind. Thus the plasma in coronal holes has lower density than that in other coronal regions due to the continuous expansion of the solar wind. The coronal-hole boundaries are often used to evaluate the quality of a numerical MHD model for the steady solar wind. Fig. 3 displays the synoptic maps of coronal holes at the base of the corona obtained from observations of the Extreme ultraviolet Imaging Telescope (EIT) onboard SOHO (left panel) and from the

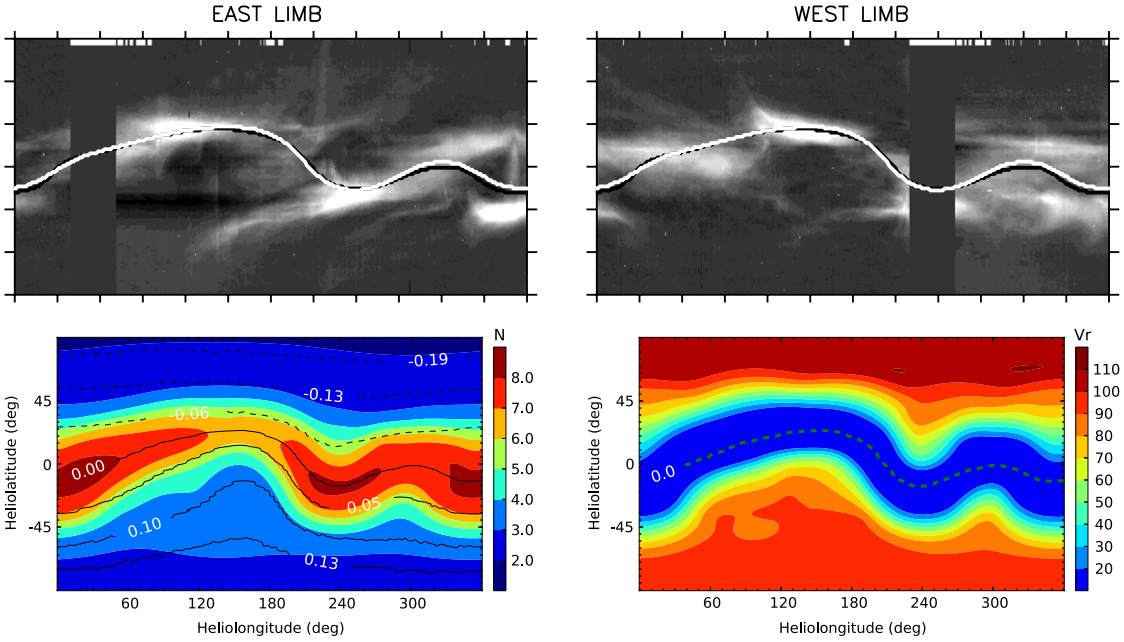

Fig. 4. Synoptic maps at 2.5 R_S for CR 2060. The first row indicates the white-light polarized brightness at the east (*left*) and west (*right*) limbs from SOHO/LASCO-C2. In the first row, the black lines denote the magnetic neutral lines from the MHD model and the white lines from the PFSS model. In the second row, the left panel overlays the isolines of the radial magnetic field [Gauss] on the contour map of the simulated number density N [10^5 cm^{-3}] and the right one is the pseudo-color image of the radial speed v_r [km s^{-1}]. In the left panel, the dashed lines stand for inward radial magnetic field and the solid ones outward radial magnetic field. The dashed lines in the right panel denote the magnetic neutral lines.

model solution (right panel) for CR 2060. The black vertical stripe in the left panel represents data gaps. In the right panel, the modeled coronal holes (the open-field regions) are displayed in white color and the other regions (the closed-field regions) with green. The open- and closed-field regions are determined by tracing the magnetic field lines from 6 R_S back to the photosphere. Both the observations and the model solution show that equatorward boundary of the northern polar coronal hole ranges between 55° and 73° N. As for the southern polar hole, seen from the simulated results, its equatorward boundary lies roughly along the latitudinal line of 70° S except two large extending holes between 70° and 190° and around 300°. Though the EIT observation cannot give the global view because of data gap, Riley et al. [143] and Yang et al. [58] gave similar coronal-hole boundaries. In fact, the southern polar coronal hole could not be clearly seen from SOHO and STEREO (Solar TErrestrial RElations Observatory) because they orbited near their highest points in heliographic latitude during CR 2060. In additional to the polar coronal holes, the isolated equatorial holes around $(\theta, \phi) = (10°, 240°)$ and $(0°, 350°)$ are also reproduced with a relatively small size in the model solution. Mid-latitude or equatorial holes were rarely present in the previous solar minima. However, their presence has become an uncommon observational feature during the 2008 solar minimum, which has attracted the interests of many solar physicists and heliophysicists, e.g., [28,54,144–148]. To sum up, our simulation has basically captured the open–closed boundary.

In Fig. 4, we present the synoptic maps of white-light polarized brightness (pB) at the east (left) and west (right) limbs observed by the Large Angle Spectrometric Coronagraph (LASCO) C2 on board SOHO and the synoptic maps of the proton number density and the radial velocity on the surface of 2.5 radii. The bright areas in pB images often indicate that there are high-density structures near the sky plane along the line of sight through these points. This figure shows that both the MHD and PFSS models give almost the same magnetic neutral line (MNL) characterized by two peaks roughly at $\phi = 150°$ and $\phi = 310°$ and a trough at $\phi = 240°$, which indicates there exists the presence of the tilting and warping of the MNL and also the curving of the streamer belt during this period. The peak of the MNL is located just next to the southern coronal hole and the trough next to the isolated equatorial coronal hole. Fig. 4 also shows that the MNL is surrounded by regions of high density and low speed plasma flow, which is consistent with the distribution of the pB enhanced regions observed by LASCO/C2 and the simulation conducted by Feng et al. [31]. It should be noted that the high-density structures are also present in the regions far away from the MNL shown in the upper panels of Fig. 4 and are associated to unipolar streamers [143].

Fig. 5 presents the white-light pB images from 2.3 to 6 R_S recorded by SOHO/LASCO C2 (left panel) and synthesized from the simulation result (right panel) at $\phi = 0°$–$180°$ for CR 2060. The upper left panel in Fig. 6 displays the simulated magnetic field topology projected on the meridional planes from 1 to 11 R_S, which is color-coded by the magnitude of the radial speed. The upper right panel exhibits the simulated current sheet from 1 to 6 R_S. The bottom panel in Fig. 6 is the simulated radial solar-wind speed on the meridional plane from 1 to 20 R_S, where the black quadrilaterals denote the grid blocks. In Fig. 5, the bright areas span wide latitudes at both limbs. Comparing with Figs. 4 and 6, we can find that the southeastern and northwestern parts of the bright structures in Fig. 5 are correspondent to the magnetic neutral line, and the northeastern and southwestern parts are probably associated with the edges of the unipolar streamers or pseudo-streamers roughly centered at Longitudes 315° and 225°, which can be seen more clearly in Fig. 5 of Riley et al. [143]. Unipolar streamers separate holes of the same polarity, and hence contain a double loop structure and emanate low-speed solar wind in interplanetary space [143]. Other causes for the diffusive bright structures are attributed to the high-density regions in different longitudes projected onto the sky plane and the transient event on Day 228 recorded by STEREO.

7.2. Interplanetary solar wind

In order to consider the solar wind structure in interplanetary space and the in-situ measurements, we present the model solutions at the surfaces of 20 R_S and 215 R_S in Fig. 7 and compare the

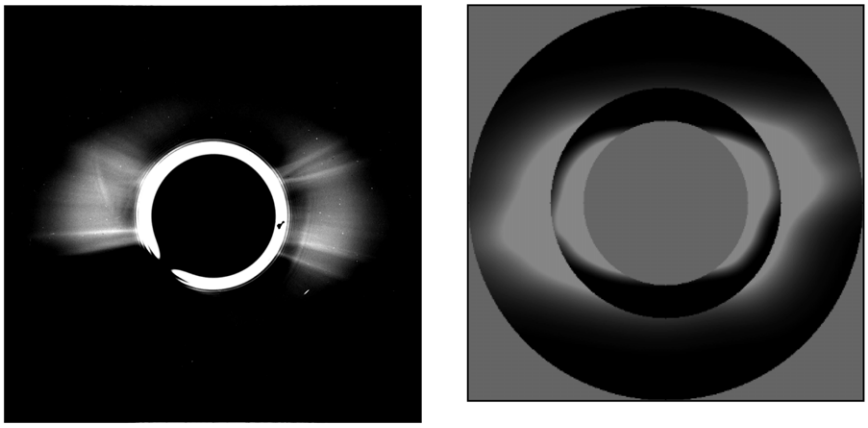

Fig. 5. The coronal observation and the simulation result on the meridional plane at $\phi = 0°$–$180°$ for CR 2060. The left and right panels are the white-light pB images from 2.3 to 6 R_S recorded by SOHO/LASCO-C2 and computed from the simulation, respectively.

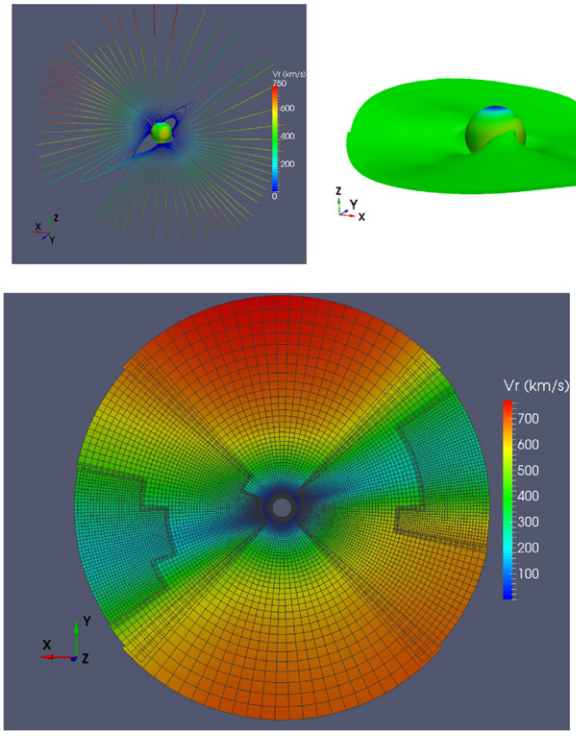

Fig. 6. The simulated coronal results for CR 2060. The upper left panel is the simulated magnetic field topology projected on the meridional plane at $\phi = 0°$–$180°$ from 1 to 11 R_S, and the magnetic field lines are color-coded by the magnitude of the radial speed. The upper right panel exhibits the simulated current sheet from 1 to 6 R_S. The bottom panel is the simulated radial solar-wind speed on the meridional plane at $\phi = 0°$–$180°$ from 1 to 20 R_S, where the black quadrilaterals denote the grid blocks. The overset grids between components can be easily seen near the lines of $\theta = \frac{\pi}{4}$ and $\frac{3\pi}{4}$.

modeled temporal profiles of the solar wind parameter with the in-situ measurements in Fig. 8. Fig. 7 shows that the first peak of HCS roughly centered around at $\phi = 150°$ at 2.5 R_S shifts to $\phi = 140°$ at 20 R_S and $\phi = 80°$ at 215 R_S due to the solar rotation, while the trough at $\phi = 240°$ shifts to $\phi = 230°$ at 20 R_S and $\phi = 165°$ at 215 R_S. What is more, the highest mass-flux regions are coincident with the locations of HCS and the low-speed solar wind ($v_r < 550$ km/s) covers about 50°–65° in latitude, unlike the low-speed solar wind only spanned 40° in the previous solar minimum. These are consistent with the studies on the unusual solar minimum caused by the weaker polar photospheric magnetic field [31,54,148]. In addition, the upper right panel in Fig. 7 shows that the finer AMR grids resolve the interfaces between high-speed and low-speed streams very well. Seen from Fig. 8, the model matches the stream structure reasonably well. The model solution shows that the initial long-duration of slow wind is followed by a strong and steep high-speed stream on Day 12, August 26, 2008, which is one day earlier than the observation. The second modeled high-speed stream rises on almost the same date as observed, but declines so slowly that the solution misses the low-speed stream between the second and third high-speed streams. Both the modeled and the measured polarities of the radial magnetic field during this interval switch from inward to outward around August 30, 2008 and are in reasonable agreement except on the first 4 days and the last two days. The smaller-scale reversals missed by the model's results probably represent waves and/or turbulence, which are not included in the MHD model. Like many other numerical MHD models, the radial field strength obtained from the model solution here is only one-third to one-half of the observation, which cannot be improved only by means of high-resolution grids as other researchers noted Riley et al. [28].

8. Conclusions

In this paper, a new adaptive mesh refinement implementation of SIP-CESE MHD model is established directly in hexahedral meshes with the aid of the parallel AMR package PARAMESH available at http://sourceforge.net/projects/paramesh/. Numerical validation through CR 2060 is carried out by the newly developed 3D SIP-AMR-CESE MHD model. The numerical simulation has reproduced a lot of features near the Sun during the simulated CR 2060. The numerical results in CR 2060 have some distinctions from the previous minima demonstrated by other researchers [54,149]. Many observed interplanetary structures have also been reproduced by the simulations. At 1 AU, the steady solutions from our model have captured the observed changing trends of the solar wind parameters for this CR except that some peaks of solar wind speed decline more slowly and arrive no more than 3 days earlier than observed. In addition, the IMF polarities and their changes are captured by our simulations with fairly good accuracy. These simulated features by this new implementation confirm to those obtained by AMR implementation in the context of reference coordinates [31]. Here, decomposition of a spherical surface grid (θ, ϕ) into six identical components with piling up the radial direction, combined with a simple radial decomposition of the spherical shell computational domain, can be managed to yield very good load balancing since the processor workload and the communication load are very similar for each processor. However, this is not necessarily true for other grids, in particular AMR in Cartesian coordinates.

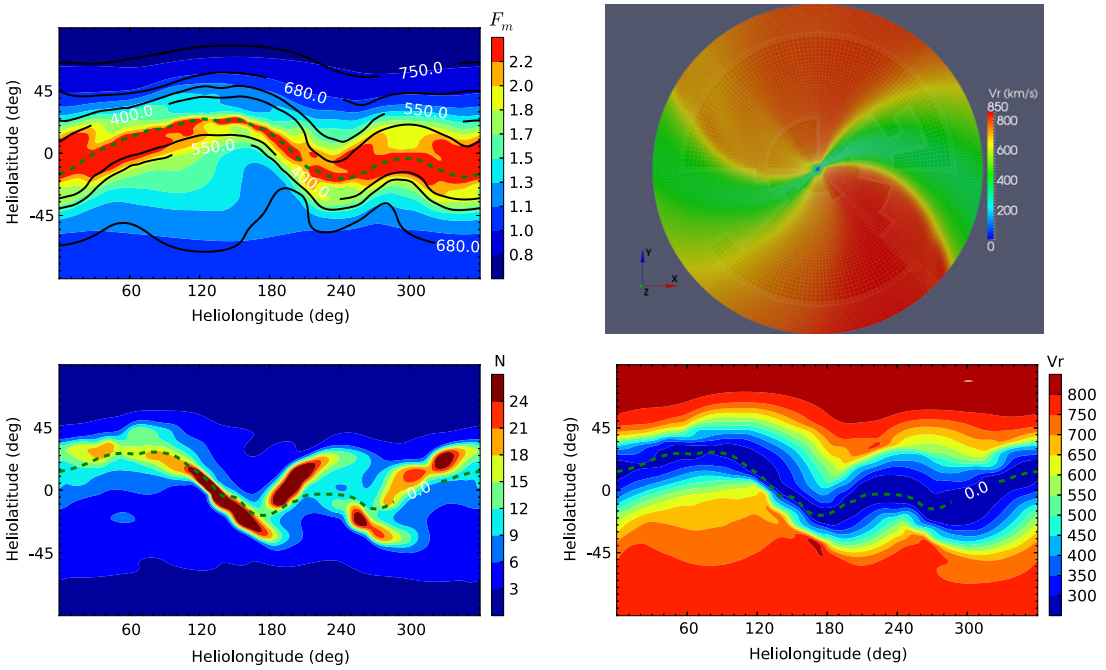

Fig. 7. The simulated steady solution in interplanetary space from the MHD model for CR 2060. The top row displays the isolines of the radial speed [v_r: km s^{-1}] superimposed on the synoptic pseudo-color image of the mass flux density [F_m: 10^8 km s^{-1} cm$^{-3}R_s^2$] at 20 R_S (*left*), and the pseudo-color image of the radial velocity in the solar equatorial plane (*right*). The bottom row shows the synoptic contours of the simulated proton number density [N: cm^{-3}] (*left*) and v_r [km s^{-1}] (*right*) at 215 R_S. Here, the dashed lines denote the magnetic neutral lines.

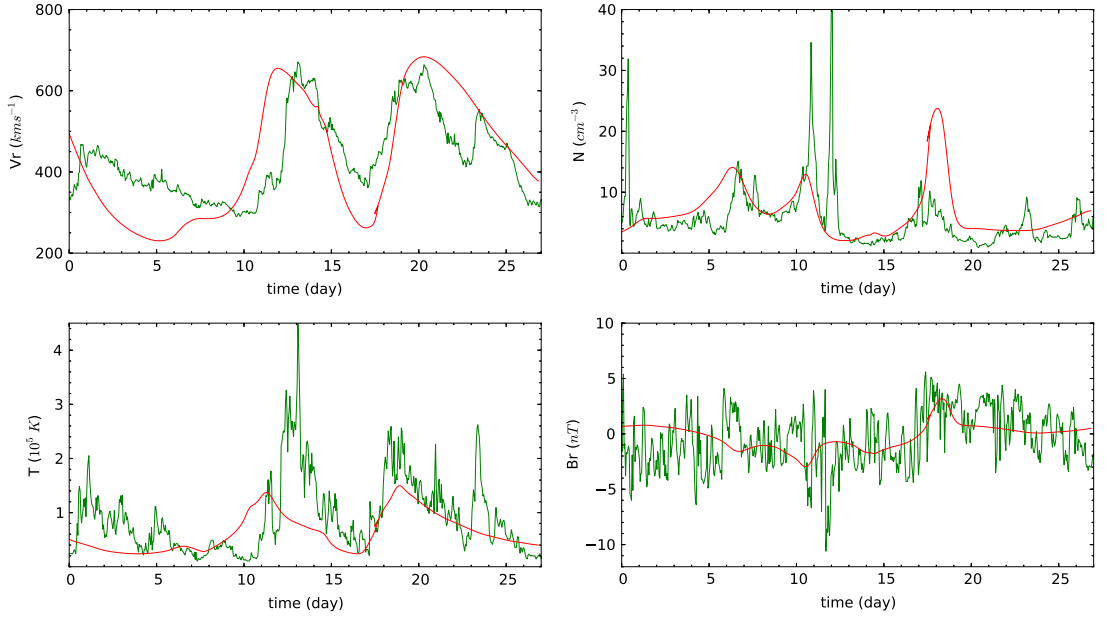

Fig. 8. The calculated MHD steady state at 1 AU for CR 2060 with comparisons of the one-hour averaged OMNI data near 1 AU for radial solar-wind speed [v_r], number density [N], temperature [T], and radial magnetic field [B_r]. Here, the green lines denote the observations and the red lines represent the numerical results. (For interpretation of the references to colour in this figure legend, the reader is referred to the web version of this article.)

On the one hand, our model can reproduce the shape and distribution of the polar coronal holes and the presence of the equatorial holes most of the observed features for CR 2060. It can also achieve the basically consistent temporal profiles of solar wind parameter at 1 AU with the in-situ measurements. These features are essentially determined by the photospheric magnetic fields, especially their dipole and quadrupole components [150] and the polar open fields [151], and they are also in agreement with the previous studies [31,58,143]. On the other hand, we should also note that there exist some differences between the numerical results and observations, such as the magnitude of radial magnetic fields and arrival times of the high-speed stream at the Earth. For the purpose of improving the numerical results to better capture the structures of the heliosphere during specific time periods, it may be reasonable to conduct simulations using high time-cadence photospheric magnetograms to drive the model just as done by Riley et al. [28], Feng et al. [55], Yang et al. [58], and Feng et al. [60]. Another remedy may lie in running different cases using synoptic maps from different instruments and choosing the solution that best matches the observations under study. Additionally, the Air force Data Assimilative Photospheric flux Transport (ADAPT) model [152–155] can assimilate different observations into surface flux model and

thus provide more instantaneous snapshots of the global photospheric field distribution than those by traditional methods. The ADAPT results by incorporating the high-quality observations from SOHO/MDI and SDO/HMI [156] will be promising to improve the input of the MHD simulations.

Computationally speaking, the huge computation requirement in global MHD simulations is also the main problem that needs to be solved, and high-performance computational models are needed to make the real-time or faster than real-time numerical prediction of adverse space weather events and their influence on the geospace environment [47,157,158]. With the recent development of modern graphics processing units (GPUs), it is possible to fully exploit the computing power in a heterogeneous CPU/GPU cluster and significantly improves the overall performance of global MHD simulations in a more efficient manner as shown by Feng et al. [47,157] and Wong et al. [158]. This kind of GPU-accelerated implementation will be a promising route to speedup our code in the future.

Acknowledgments

The work is jointly supported by the National Basic Research Program (973 program) under grant 2012CB825601, the Knowledge Innovation Program of the Chinese Academy of Sciences (KZZD-EW-01-4), the National Natural Science Foundation of China (41031066, 41231068, 41274192, 41174150, and 41374176), and the Specialized Research Fund for State Key Laboratories. The numerical calculation has been completed on our SIGMA Cluster computing system. The PARAMESH software used in this work was developed at the NASA Goddard Space Flight Center and Drexel University under NASA's HPCC and ESTO/CT projects and under grant NNG04GP79G from the NASA/AISR project. Wilcox Solar Observatory data used in this study were obtained via http://wso.stanford.edu. The Wilcox Solar Observatory is currently supported by NASA. SOHO is a project of international cooperation between ESA and NASA. The OMNI data is obtained from the GSFC/SPDF OMNIWeb interface http://omniweb.gsfc.nasa.gov. We are appreciated for our referee's constructive suggestions for the improvement.

References

[1] Z. Mikić, J.A. Linker, D.D. Schnack, R. Lionello, A. Tarditi, Phys. Plasmas 6 (1999) 2217–2224.
[2] R. Lionello, J.A. Linker, Z. Mikić, Astrophys. J. 690 (2009) 902–912.
[3] P. Riley, J.A. Linker, Z. Mikić, R. Lionello, S.A. Ledvina, J.G. Luhmann, Astrophys. J. 653 (2006) 1510–1516.
[4] I.I. Roussev, et al., Astrophys. J. Lett. 595 (1) (2003) L57.
[5] G. Tóth, et al., J. Geophys. Res. 110 (A9) (2005) A12226.
[6] O. Cohen, I.V. Sokolov, I.I. Roussev, T.I. Gombosi, J. Geophys. Res. 113 (A12) (2008) A03104.
[7] N. Lugaz, C. Downs, K. Shibata, I.I. Roussev, A. Asai, T.I. Gombosi, Astrophys. J. 738 (2) (2011) 127.
[8] G. Tóth, B. van der Holst, I.V. Sokolov, D.L. De Zeeuw, T.I. Gombosi, F. Fang, W.B. Manchester, X. Meng, D. Najib, K.G. Powell, Q.F. Stout, A. Glocer, Y.-J. Ma, M. Opher, J. Comput. Phys. 231 (2012) 870–903.
[9] A.V. Usmanov, M.L. Goldstein, J. Geophys. Res. 111 (A10) (2006) A07101.
[10] A.V. Usmanov, W.H. Matthaeus, B.A. Breech, M.L. Goldstein, Astrophys. J. 727 (2) (2011) 84.
[11] A.V. Usmanov, M.L. Goldstein, W.H. Matthaeus, Astrophys. J. 754 (1) (2012) 40.
[12] X.S. Feng, Y.F. Zhou, S.T. Wu, Astrophys. J. 655 (2007) 1110.
[13] A. Nakamizo, T. Tanaka, Y. Kubo, S. Kamei, H. Shimazu, H. Shinagawa, J. Geophys. Res. 114 (A13) (2009) 7109.
[14] B. van der Holst, W.B. Manchester, R.A. Frazin, A.M. Vásquez, G. Tóth, T.I. Gombosi, Astrophys. J. 725 (1) (2010) 1373.
[15] X.S. Feng, L.P. Yang, C.Q. Xiang, S.T. Wu, Y.F. Zhou, D.K. Zhong, Astrophys. J. 723 (2010) 300.
[16] A. Taktakishvili, A. Pulkkinen, P. MacNeice, M. Kuznetsova, M. Hesse, D. Odstrcil, Space Weather 90 (2011) 6002.
[17] T. Tanaka, J. Comput. Phys. 111 (1994) 381–390.
[18] T. Tanaka, J. Geophys. Res. 100 (A7) (1995) 12057.
[19] P. Janhunen, K.E.J. Koskinen, T.I. Pulkinen, in: E.J. Rolfe, B. Kaldeich (Eds.), International Conference on Substorms, vol. 389, ESA Special Publication, 1996, p. 205.
[20] K.G. Powell, P.L. Roe, T.J. Linde, T.I. Gombosi, D.L. De Zeeuw, J. Comput. Phys. 154 (1999) 284–309.
[21] J.G. Lyon, Science 288 (5473) (2000) 1987–1991.
[22] J. Lyon, J. Fedder, C. Mobarry, J. Atmos. Sol.-Terr. Phys. 66 (15–16) (2004) 1333–1350.
[23] J. Raeder, Y. Wang, T. Fuller-Rowell, H. Singer, Solar Phys. 204 (2001) 323–337.
[24] T. Ogino, J. Geophys. Res. 91 (1986) 6791–6806.
[25] T. Ogino, Concur. Comput. Pract. Exper. 14 (8–9) (2002) 631–646.
[26] Y.Q. Hu, X.C. Guo, C. Wang, J. Geophys. Res. (Space Phys.) 112 (A11) (2007) 7215.
[27] P. Riley, R. Lionello, J.A. Linker, Z. Mikic, J. Luhmann, J. Wijaya, Solar Phys. 274 (2011) 361–377.
[28] P. Riley, J.A. Linker, R. Lionello, Z. Mikic, J. Atmos. Sol.-Terr. Phys. 83 (2012) 1–10.
[29] X.S. Feng, S.H. Zhang, C.Q. Xiang, L.P. Yang, C.W. Jiang, S.T. Wu, Astrophys. J. 734 (2011) 50.
[30] M. Jin, W.B. Manchester, B. van der Holst, J.R. Gruesbeck, R.A. Frazin, E. Landi, A.M. Vasquez, P.L. Lamy, A. Llebaria, A. Fedorov, G. Toth, T.I. Gombosi, Astrophys. J. 745 (1) (2012) 6.
[31] X.S. Feng, L.P. Yang, C.Q. Xiang, C.W. Jiang, X.P. Ma, S.T. Wu, D.K. Zhong, Y.F. Zhou, Solar Phys. 279 (2012) 207–229.
[32] D. Odstrčil, M. Dryer, Z. Smith, J. Geophys. Res. 1011 (1996) 19973–19986.
[33] G. Tóth, D. Odstrčil, J. Comput. Phys. 128 (1996) 82–100.
[34] K. Hayashi, Astrophys. J. Suppl. Ser. 161 (2005) 480.
[35] K. Hayashi, J. Geophys. Res.: Space Phys. 118 (11) (2013) 6889–6906.
[36] T.I. Gombosi, D.L. de Zeeuw, K.G. Powell, et al., in: J. Büchner, C. Dum, M. Scholer (Eds.), Space Plasma Simulation, in: Lecture Notes in Physics, vol. 615, Springer Verlag, Berlin, 2003, pp. 247–274.
[37] C. Downs, I.I. Roussev, B. van der Holst, N. Lugaz, I.V. Sokolov, T.I. Gombosi, Astrophys. J. 712 (2) (2010) 1219.
[38] R. Lionello, Z. Mikić, D.D. Schnack, J. Comput. Phys. 140 (1998) 172–201.
[39] J.A. Linker, Z. Mikić, D.A. Biesecker, R.J. Forsyth, S.E. Gibson, A.J. Lazarus, A. Lecinski, P. Riley, A. Szabo, B.J. Thompson, J. Geophys. Res. 104 (1999) 9809–9830.
[40] J. Kleimann, A. Kopp, H. Fichtner, R. Grauer, Ann. Geophys. 27 (2009) 989–1004.
[41] P. Janhunen, J. Comput. Phys. 160 (2000) 649–661.
[42] T. Miyoshi, N. Terada, Y. Matsumoto, K. Fukazawa, T. Umeda, K. Kusano, IEEE Trans. Plasma Sci. 38 (2010) 2236–2242.
[43] M. Dryer, Asian J. Phys. 16 (2007) 97–121.
[44] M.J. Aschwanden, L.F. Burlaga, M.L. Kaiser, C.K. Ng, D.V. Reames, M.J. Reiner, T.I. Gombosi, N. Lugaz, W. Manchester, I.I. Roussev, T.H. Zurbuchen, C.J. Farrugia, A.B. Galvin, M.A. Lee, J.A. Linker, Z. Mikić, P. Riley, D. Alexander, A.W. Sandman, J.W. Cook, R.A. Howard, D. Odstrčil, V.J. Pizzo, J. Kóta, P.C. Liewer, J.G. Luhmann, B. Inhester, R.W. Schwenn, S.K. Solanki, V.M. Vasyliunas, T. Wiegelmann, L. Blush, P. Bochsler, I.H. Cairns, P.A. Robinson, V. Bothmer, K. Kecskemety, A. Llebaria, M. Maksimovic, M. Scholer, R.F. Wimmer-Schweingruber, Space Sci. Rev. 136 (2008) 565–604.
[45] J. Watermann, et al., Space Sci. Rev. 147 (2009) 233–270.
[46] X.S. Feng, C.Q. Xiang, D.K. Zhong, Sci. Sin-Terrae 41 (2011) 1–28 (in Chinese).
[47] X.S. Feng, C.Q. Xiang, D.K. Zhong, Sci. China: Earth Sci. 56 (2013) 1864–1880.
[48] Y.Q. Hu, X.S. Feng, S.T. Wu, W.B. Song, J. Geophys. Res. 113 (A12) (2008) 3106.
[49] Y.-F. Zhou, X.-S. Feng, S.-T. Wu, Chin. Phys. Lett. 25 (2008) 790–793.
[50] Y.F. Zhou, X.S. Feng, Sci. China Ser. E: Technol. Sci. 51 (2008) 1600–1610.
[51] X.S. Feng, Y. Zhang, L.P. Yang, S.T. Wu, M. Dryer, J. Geophys. Res. 114 (A13) (2009) 10103.
[52] C.W. Jiang, X.S. Feng, J. Zhang, D.K. Zhong, Solar Phys. 267 (2010) 463–491.
[53] C.W. Jiang, X.S. Feng, Y.L. Fan, C.Q. Xiang, Astrophys. J. 727 (2011) 101.
[54] L.P. Yang, X.S. Feng, C.Q. Xiang, S.H. Zhang, S.T. Wu, Solar Phys. 271 (2011) 91–110.
[55] X.S. Feng, L.P. Yang, C.Q. Xiang, Y. Liu, X.P. Zhao, S.T. Wu, in: N.V. Pogorelov, J.A. Font, E. Audit, G.P. Zank (Eds.), Numerical Modeling of Space Plasma Slows (ASTRONUM 2011), in: Astronomical Society of the Pacific Conference Series, vol. 459, 2012, p. 202.
[56] C.W. Jiang, X.S. Feng, Astrophys. J. 749 (2) (2012) 135.
[57] Y.F. Zhou, X.S. Feng, S.T. Wu, D. Du, F. Shen, C.Q. Xiang, J. Geophys. Res. 117 (A16) (2012) 1102.
[58] L.P. Yang, X.S. Feng, C.Q. Xiang, Y. Liu, X.P. Zhao, S.T. Wu, J. Geophys. Res. 117 (A16) (2012) 8110.
[59] C.W. Jiang, X.S. Feng, C.Q. Xiang, Astrophys. J. 755 (1) (2012) 62.
[60] X.S. Feng, C.W. Jiang, C.Q. Xiang, X.P. Zhao, S.T. Wu, Astrophys. J. 758 (1) (2012) 62.
[61] L.P. Yang, X.S. Feng, C.Q. Xiang, C.W. Jiang, Chin. Phys. Lett. 28 (3) (2011) 039601.
[62] C.W. Jiang, X.S. Feng, S.T. Wu, Q. Hu, Astrophys. J. Lett. 771 (2) (2013) L30.
[63] C.W. Jiang, X.S. Feng, Astrophys. J. 769 (2) (2013) 144.
[64] Y.F. Zhou, X.S. Feng, J. Geophys. Res.: Space Phys. 118 (10) (2013) 6007–6018.
[65] S.T. Wu, W.P. Guo, D.J. Michels, L.F. Burlaga, J. Geophys. Res. 104 (1999) 14789–14802.
[66] B. Marder, J. Comput. Phys. 68 (1) (1987) 48–55.
[67] B. van der Holst, R. Keppens, J. Comput. Phys. 226 (1) (2007) 925–946.

[68] R. Keppens, Z. Meliani, A. van Marle, P. Delmont, A. Vlasis, B. van der Holst, J. Comput. Phys. 231 (3) (2012) 718–744.
[69] A. Dedner, F. Kemm, D. Kröner, C. Munz, T. Schnitzer, M. Wesenberg, J. Comput. Phys. 175 (2002) 645–673.
[70] A. Mignone, P. Tzeferacos, J. Comput. Phys. 229 (6) (2010) 2117–2138.
[71] E. Endeve, E. Leer, T.E. Holzer, Astrophys. J. 589 (2003) 1040–1053.
[72] C.N. Arge, D. Odstrcil, V.J. Pizzo, L.R. Mayer, in: M. Velli, R. Bruno, F. Malara, B. Bucci (Eds.), Solar Wind Ten, in: American Institute of Physics Conference Series, vol. 679, 2003, p. 190.
[73] M.J. Owens, C.N. Arge, H.E. Spence, A. Pembroke, J. Geophys. Res. 110 (A9) (2005) A12105.
[74] S.-C. Chang, J. Comput. Phys. 119 (2) (1995) 295–324.
[75] S.-C. Chang, X.-Y. Wang, C.-Y. Chow, J. Comput. Phys. 156 (1) (1999) 89–136.
[76] S.-C. Chang, X.-Y. Wang, W.-M. To, J. Comput. Phys. 165 (1) (2000) 189–215.
[77] C.Y. Loh, S.-C. Chang, L.S. Hultgren, Amer. Inst. Aeronaut. Astronaut. 39 (2001) 794–801.
[78] Z. Zhang, S.T.J. Yu, S. Chang, J. Comput. Phys. 175 (2002) 168–199.
[79] M. Vinokur, J. Comput. Phys. 81 (1) (1989) 1–52.
[80] S.T. Yu, S.C. Chang, Treatments of stiff source terms in conservation laws by the method of space–time conservation element and solution element, AIAA paper 97-0435.
[81] Z.C. Zhang, S.T. Yu, Shock capturing without Riemann solver—A modified space–time CE/SE method for conservation laws, AIAA paper 99-0904.
[82] Z.C. Zhang, S.T. John Yu, S.C. Chang, A. Himansu, P. Jorgenson, A modified space–time CE/SE method for Euler and Navier–Stokes equations, AIAA paper 99-3277.
[83] M. Neugebauer, Rev. Geophys. 37 (1) (1999) 107–126.
[84] P. MacNeice, K.M. Olson, C. Mobarry, R. de Fainchtein, C. Packer, Comput. Phys. Commun. 126 (2000) 330–354.
[85] M. Sun, K. Takayama, A solution-adaptive technique using unstructured hexahedral grids, AIAA-2001-2656.
[86] M.J. Berger, P. Colella, J. Comput. Phys. 82 (1989) 64–84.
[87] M. Sun, Numerical and experimental studies of shock wave interaction with bodies, Ph.D. Thesis. 1998. URL http://rainbow.ifs.tohoku.ac.jp/~swrc/thesis/thesis0.pdf.
[88] D.S. Balsara, D. Spicer, J. Comput. Phys. 148 (1) (1999) 133–148.
[89] K. Waagan, J. Comput. Phys. 228 (2009) 8609–8626.
[90] F.G. Fuchs, A.D. McMurry, S. Mishra, N.H. Risebro, K. Waagan, Commun. Comput. Phys. 7 (3) (2010) 1–30.
[91] T. Ogino, R.J. Walker, Geophys. Res. Lett. 11 (1984) 1018.
[92] B. Parent, J. Comput. Phys. 231 (1) (2012) 173–189.
[93] D.S. Balsara, J. Comput. Phys. 231 (22) (2012) 7504–7517.
[94] P. Colella, P.R. Woodward, J. Comput. Phys. 54 (1) (1984) 174–201.
[95] W. Dai, P.R. Woodward, J. Comput. Phys. 142 (2) (1998) 331–369.
[96] T.A. Gardiner, J.M. Stone, J. Comput. Phys. 205 (2) (2005) 509–539.
[97] T.A. Gardiner, J.M. Stone, J. Comput. Phys. 227 (8) (2008) 4123–4141.
[98] G.-S. Jiang, C.-C. Wu, J. Comput. Phys. 150 (1999) 561–594.
[99] A. Majda, S. Osher, Commun. Pure Appl. Math. 30 (6) (1977) 671–705.
[100] R. Donat, S. Osher, Comput. Methods Appl. Mech. Engrg. 80 (1–3) (1990) 59–64.
[101] J. Casper, M.H. Carpenter, SIAM J. Sci. Comput. 19 (3) (1998) 813–828.
[102] J.A. Greenough, W.J. Rider, J. Comput. Phys. 196 (2004) 259–281.
[103] W. Rider, J. Kamm, in: C. Groth, D.W. Zingg (Eds.), Computational Fluid Dynamics 2004, Springer, Berlin Heidelberg, 2006, pp. 401–405.
[104] D. Tafti, Comput. & Fluids 25 (7) (1996) 647–665.
[105] L. Lehner, S.L. Liebling, O. Reula, Class. Quantum Gravity 23 (16) (2006) S421.
[106] S.T. Li, J.M. Hyman, Adaptive mesh refinement for finite difference WENO schemes, Tech. Rep. LA-UR-03-8927, Los Alamos National Lab, 2003.
[107] C. Shen, J.-M. Qiu, A. Christlieb, J. Comput. Phys. 230 (2011) 3780–3802.
[108] M. Yalim, D.V. Abeele, A. Lani, T. Quintino, H. Deconinck, J. Comput. Phys. 230 (15) (2011) 6136–6154.
[109] J.U. Brackbill, D.C. Barnes, J. Comput. Phys. 35 (3) (1980) 426–430.
[110] C.R. Evans, J.F. Hawley, Astrophys. J. 332 (1988) 659–677.
[111] D.S. Balsara, D.S. Spicer, J. Comput. Phys. 149 (1) (1999) 270–292.
[112] U. Ziegler, J. Comput. Phys. 230 (4) (2011) 1035–1063.
[113] D.S. Balsara, Astrophys. J. Suppl. Ser. 151 (2004) 149–184.
[114] D.S. Balsara, Astrophys. J. Suppl. Ser. 116 (1) (1998) 133.
[115] D. Balsara, Astrophys. J. Suppl. Ser. 132 (1) (2001) 83.
[116] D.S. Balsara, J. Comput. Phys. 174 (2001) 614–648.
[117] M. Zhang, I. Blankson, S.-C. Chang, S.-C. Lin, S.-T.J. Yu, Amer. Inst. Aeronaut. Astronaut. 42 (2004) 2605–2608.
[118] M. Zhang, S.-T. John Yu, S.-C. Henry Lin, S.-C. Chang, I. Blankson, J. Comput. Phys. 214 (2006) 599–617.
[119] X.S. Feng, Y.Q. Hu, F.S. Wei, Solar Phys. 235 (2006) 235–257.
[120] Y.X. Liu, Z. Ji, X.S. Feng, Y.F. Zhou, Chin. J. Space Sci. 30 (3) (2010) 211–220.
[121] S. Qamar, S. Mudasser, Appl. Numer. Math. 60 (6) (2010) 587–606.
[122] L. Jameson, J. Sci. Comput. 18 (2003) 1–24.
[123] K.-G. Powell, P.L. Roe, R.S. Myong, D.D. Aee, An upwind scheme for magnetohydrodynamics, AIAA 95-1704-CP (1995) 661–671.
[124] R.S. Myong, P.L. Roe, J. Comput. Phys. 147 (1998) 545–567.
[125] A.L. Zachary, P. Colella, J. Comput. Phys. 99 (1992) 341–347.
[126] P.L. Roe, Annu. Rev. Fluid Mech. 18 (1986) 337–365.
[127] J.L. Steger, R.F. Warming, J. Comput. Phys. 40 (1981) 263–293.
[128] K. Gurski, SIAM J. Sci. Comput. 25 (6) (2004) 2165–2187.
[129] S. Li, J. Comput. Phys. 203 (2005) 344–357.
[130] T. Miyoshi, K. Kusano, J. Comput. Phys. 208 (2005) 315–344.
[131] F.G. Fuchs, S. Mishra, N.H. Risebro, J. Comput. Phys. 228 (2009) 641–660.
[132] D.S. Balsara, J. Comput. Phys. 229 (2010) 1970–1993.
[133] R.W. MacCormack, An upwind conservation form method for ideal magnetohydrodynamics equations, AIAA Paper 99-3609, 30th Plasmadynamics and Laser Conference, Norfolk, VA, 28 June, July 1999.
[134] J. Shang, Prog. Aerosp. Sci. 40 (2004) 173–197.
[135] G. Tóth, X. Meng, T.I. Gombosi, A.J. Ridley, J. Geophys. Res. 116 (A15) (2011) A07211.
[136] H.C. Yee, B. Sjögreen, J. Comput. Phys. 225 (1) (2007) 910–934.
[137] Y.-Q. Shen, G.C. Zha, M.A. Huerta, E-CUSP Scheme for the equations of magnetothydrodynamics with high order WENO scheme, AIAA 2011-383, 49th AIAA Aerospace Sciences Meeting including the New Horizons Forum and Aerospace Exposition 150 (2011) 561–594.
[138] P.L. Roe, D.S. Balsara, SIAM J. Appl. Math. 56 (1996) 57–67.
[139] P. Cargo, G. Gallice, J. Comput. Phys. 136 (1997) 446–466.
[140] Y. Shen, G. Zha, M.A. Huerta, J. Comput. Phys. 231 (19) (2012) 6233–6247.
[141] T.J. Poinsot, S.K. Lele, J. Comput. Phys. 101 (1992) 104–129.
[142] D.M. Pahud, V.G. Merkin, C.N. Arge, W.J. Hughes, S.M. McGregor, J. Atmos. Sol.-Terr. Phys. 83 (2012) 32–38.
[143] P. Riley, M. Stevens, J.A. Linker, R. Lionello, Z. Mikic, J.G. Luhmann, in: J. Heerikhuisen, G. Li, N. Pogorelov, G. Zank (Eds.), American Institute of Physics Conference Series, in: American Institute of Physics Conference Series, vol. 1436, 2012, pp. 337–343.
[144] D.J. McComas, R.W. Ebert, H.A. Elliott, B.E. Goldstein, J.T. Gosling, N.A. Schwadron, R.M. Skoug, Geophys. Res. Lett. 35 (2008) 18103.
[145] D. Lee, A.E. Deane, J. Comput. Phys. 228 (2009) 952–975.
[146] S.E. Gibson, J.U. Kozyra, G. de Toma, B.A. Emery, T. Onsager, B.J. Thompson, J. Geophys. Res. 114 (A13) (2009) 9105.
[147] V. Abramenko, V. Yurchyshyn, J. Linker, Z. Mikić, J. Luhmann, C.O. Lee, Astrophys. J. 712 (2010) 813.
[148] G. de Toma, C.N. Arge, Twelfth International Solar Wind Conference 1216 (2010) 679–681.
[149] M. Tokumaru, M. Kojima, K. Fujiki, K. Hayashi, Geophys. Res. Lett. 36 (2009) 9101.
[150] T.R. Sanderson, T. Appourchaux, J.T. Hoeksema, K.L. Harvey, J. Geophys. Res. 108 (A1) (2003) 1035.
[151] Y. Wang, E. Robbrecht, N.R. Sheeley, Astrophys. J. 707 (2009) 1372.
[152] C.N. Arge, C.J. Henney, J. Koller, C.R. Compeau, S. Young, D. MacKenzie, A. Fay, J.W. Harvey, Twelfth International Solar Wind Conference 1216 (2010) 343–346.
[153] C.N. Arge, C.J. Henney, J. Koller, W.A. Toussaint, J.W. Harvey, S. Young, in: N.V. Pogorelov, E. Audit, G.P. Zank (Eds.), 5th International Conference of Numerical Modeling of Space Plasma Flows (ASTRONUM 2010), in: Astronomical Society of the Pacific Conference Series, vol. 444, 2011, p. 99.
[154] C.J. Henney, W.A. Toussaint, S.M. White, C.N. Arge, Space Weather 10 (2012) 2011.
[155] C.O. Lee, C.N. Arge, D. Odstrčil, G. Millward, V. Pizzo, J.M. Quinn, C.J. Henney, Solar Phys. 285 (2013) 349–368.
[156] Y. Liu, J.T. Hoeksema, P.H. Scherrer, J. Schou, S. Couvidat, R.I. Bush, T.L. Duvall, K. Hayashi, X. Sun, X. Zhao, Solar Phys. 279 (2012) 295–316.
[157] X.S. Feng, D.K. Zhong, C.Q. Xiang, Y. Zhang, in: N.V. Pogorelov, E. Audit, G.P. Zank (Eds.), Numerical Modeling of Space Plasma Flows (ASTRONUM2012), in: Astronomical Society of the Pacific Conference Series, vol. 474, 2013, p. 131.
[158] U.-H. Wong, H.-C. Wong, Y. Ma, Comput. Phys. Commun. 185 (1) (2014) 144–152.